Driven generalized quantum Rayleigh–van der Pol oscillators: Phase localization and spectral response

A. J. Sudler, J. Talukdar, and D. Blume

Homer L. Dodge Department of Physics and Astronomy, and Center for Quantum Research and Technology, The University of Oklahoma, 440 W. Brooks Street, Norman, Oklahoma 73019, USA

Driven classical self-sustained oscillators have been studied extensively in the context of synchronization. Using the master equation, this work considers the classically driven generalized quantum Rayleigh–van der Pol oscillator, which is characterized by linear dissipative gain and loss terms as well as three nonlinear dissipative terms. Since two of the nonlinear terms break the rotational phase space symmetry, the Wigner distribution of the quantum mechanical limit cycle state of the undriven system is, in general, not rotationally symmetric. The impact of the symmetry-breaking dissipators on the long-time dynamics of the driven system are analyzed as functions of the drive strength and detuning, covering the deep quantum to near-classical regimes. Phase localization and frequency entrainment, which are required for synchronization, are discussed in detail. We identify a large parameter space where the oscillators exhibit appreciable phase localization but only weak or no entrainment, indicating the absence of synchronization. Several observables are found to exhibit the analog of the celebrated classical Arnold tongue; in some cases, the Arnold tongue is found to be asymmetric with respect to vanishing detuning between the external drive and the natural oscillator frequency.

I. INTRODUCTION

Self-sustained classical oscillators do not only contain a damping term but also a term that serves as an energy source. The competition between the nonlinear damping and linear gain (sometimes also referred to as antidamping) terms introduces, in the absence of an external sinusoidal drive, a limit cycle, i.e., a stable periodic finite-amplitude trajectory in position-momentum phase space that is approached in the large time limit regardless of the oscillator's initial conditions. The asymptotic finite-amplitude oscillations of self-sustained oscillators underlie a range of phenomena in the social sciences, economics, engineering, and the fundamental sciences, including cardiac rhythms, cell rhythms, and the synchronous blinking of fireflies and clapping of audience members [1,2].

In the classical Rayleigh oscillator, which was discussed in 1883 by Strutt and Rayleigh in the context of clocks, violin strings, and clarinet reeds, the nonlinear damping is proportional to $\dot{x}^3$ (here, x denotes the dimensionless position and $\dot{x}$ the dimensionless velocity or momentum) [3]. In the van der Pol oscillator, in contrast, the nonlinear damping term is proportional to $x^2\dot{x}$; van der Pol and co-workers applied the corresponding equation of motion in 1928 to model the human heart [4,5]. We note in passing that the van der Pol oscillator equation can be obtained from the Rayleigh oscillator equation by substitution and subsequent differentiation [6].

This work considers the quantum version of the dimensionless classical oscillator equation of motion $\ddot{x} + x = \epsilon\dot{x} - (\gamma_{2,\text{vdp}}x^2 + \gamma_{2,\text{ray}}\dot{x}^2)\dot{x}$, where ϵ quantifies the linear damping term. Our main interest lies in investigating the role of the generalized non-linear damping term, characterized by the coefficients $\gamma_{2,\text{vdp}}$ and $\gamma_{2,\text{ray}}$, in the quantum regime.

Throughout this work, we refer to the oscillator with equal nonlinear position- and momentum-dependent damping ($\gamma_{2,\text{vdp}} = \gamma_{2,\text{ray}}$) as the RvdP (Rayleigh–van der Pol) oscillator [7,8] and that with $\gamma_{2,\text{vdp}} \neq \gamma_{2,\text{ray}}$ (both coefficients finite) as the generalized RvdP oscillator. While the classical Rayleigh ($\gamma_{2,\text{vdp}} = 0$; $\gamma_{2,\text{ray}} > 0$; we use R for Rayleigh throughout), classical van der Pol ($\gamma_{2,\text{vdp}} > 0$; $\gamma_{2,\text{ray}} = 0$; we use vdP for van der Pol throughout), and classical RvdP ($\gamma_{2,\text{vdp}} = \gamma_{2,\text{ray}}$) oscillators have been investigated extensively, the quantum version of the paradigmatic rotationally invariant RvdP oscillator with nonlinear damping term proportional to $(x^2 + \dot{x}^2)\dot{x}$ was first considered in 2013–2014 [9,10]. Since then, this model has been used to study various aspects of synchronization [7–26]; moreover, its applicability for sensing has also been assessed [27].

Quantum versions of the R and vdP oscillators, both of which possess limit cycles with broken rotational phase-space symmetry, were considered by Chia *et al.* [7] and Arosh *et al.* [8]. These works presented an analysis of the quantum vdP, quantum R, and quantum RvdP oscillators and their classical counterparts. The quantum mechanical systems were found to support relaxation oscillations, a key signature of classical nonlinear systems [7]. Phase synchronization, which requires phase localization (e.g., nonrotationally symmetric Wigner function) and frequency entrainment (modification of the system's frequency from the natural harmonic oscillator to the drive frequency), in the presence of a coherent sinusoidal classical drive has been studied extensively for the quantum version of the RvdP oscillator [7,10,19,21,27]. The understanding of driven systems with unequal $\gamma_{2,\text{vdp}}$ and $\gamma_{2,\text{ray}}$, in contrast, is still in its infancy [7,8]. Moreover, the deep quantum regime, in which the system response such

as the susceptibility may—extrapolating based on the behavior found for the RvdP oscillator with vanishing linear gain [27]—deviate not only quantitatively but also qualitatively from the system response in the classical regime, has not yet been investigated systematically for the generalized RvdP oscillator.

Our main conclusions, which are derived by analyzing numerical and perturbative results of the quantum master equation, are as follows: (i) In all regimes (classical to deep quantum), the phase localization increases for fixed detuning Δ with increasing drive strength Ω for all oscillator types considered, including oscillators that may be characterized as being hybrid R-RvdP oscillators or hybrid RvdP-vdP oscillators; this conclusion—consistent with the conceptual framework of synchronization, which assumes that the drive keeps the amplitude of $\Omega = 0$ limit cycle approximately unchanged—is restricted to the weak drive strength regime. (ii) Systems with nonrotationally symmetric dissipators display in the deep quantum regime behaviors that distinguish them from the RvdP oscillator, whose dissipators are rotationally symmetric. The phase localization, e.g., depends for fixed Ω on the sign of the detuning Δ and may vary no-monotonically as Δ increases or decreases from 0. (iii) The power spectrum in frequency space is determined for several drive strengths and detunings. Phase localization is observed over a much larger parameter space than frequency entrainment. In the deep quantum regime, the spectral response is very broad and frequency entrainment is either absent or extremely weak. (iv) The modification of the limit cycle amplitude by the external drive, relative to that of the drive-free system, is quantified through a deformation parameter $\bar{D}$. The deformation parameter displays, just as the number of excitations $\bar{N}$ and phase localization measure $\bar{S}_q$, Arnold tongue-like characteristics. (v) For a large parameter space, we observe phase localization but no frequency entrainment, indicating the absence of quantum synchronization. We note that many references (see, e.g., Ref. [21]) refer to the measure S_q employed in our work as phase synchronization as opposed to phase localization; we refrain from referring to S_q as phase synchronization since—in our definition—phase synchronization requires phase locking and frequency entrainment.

The remainder of this paper is organized as follows. Section II introduces the master equation, reviews the connection between the master equation and the classical equations of motion, and discusses the observables considered in this work. Results as functions of the detuning and strength of the external drive, and their interpretation, are presented in Sec. III. Finally, Sec. IV summarizes. Technical details related to the master equation in the rotating frame and a comparison of different phase localization measures are relegated to two appendices.

II. THEORETICAL FRAMEWORK

A. Quantum systems under study: Master equation

In the laboratory frame (i.e., the "non-rotating frame"), the master equation for the density matrix $\hat{\rho}$ of the generalized quantum RvdP oscillator in scaled dimensionless units reads [8]

$$
\dot{\hat{\rho}} = -\iota[\hat{H}, \hat{\rho}] + \gamma_1^+ \hat{\mathcal{D}}[\hat{a}^\dagger](\hat{\rho}) + \gamma_1^- \hat{\mathcal{D}}[\hat{a}](\hat{\rho})
$$
$$
+ \alpha \hat{\mathcal{D}}[\hat{a}\hat{a}](\hat{\rho}) + \beta \hat{\mathcal{D}}[\hat{x}\hat{a}](\hat{\rho}) + \delta \hat{\mathcal{D}}[\hat{p}\hat{a}](\hat{\rho}), \quad (1)
$$

where the operators $\hat{a}$ and $\hat{a}^\dagger$ are the bosonic annihilation and creation operators, $\hat{a}|n\rangle = \sqrt{n}|n-1\rangle$, $\hat{a}^\dagger|n\rangle = \sqrt{n+1}|n+1\rangle$, $\hat{a}^\dagger\hat{a}|n\rangle = n|n\rangle$,

$$
\hat{x} = \frac{1}{\sqrt{2}}(\hat{a} + \hat{a}^\dagger), \quad (2)
$$

and

$$
\hat{p} = \frac{1}{\sqrt{2\iota}}(\hat{a} - \hat{a}^\dagger). \quad (3)
$$

The Hamiltonian $\hat{H}$,

$$
\hat{H} = \hat{H}_0 + \hat{V}_{\text{drive}}, \quad (4)
$$

contains the dimensionless one-dimensional harmonic oscillator Hamiltonian $\hat{H}_0$,

$$
\hat{H}_0 = \hat{a}^\dagger\hat{a} \quad (5)
$$

(for convenience, the ground state energy is chosen to be equal to 0), as well as the external drive $\hat{V}_{\text{drive}}$,

$$
\hat{V}_{\text{drive}} = \Omega \sin(\omega_D t)\frac{\hat{a} + \hat{a}^\dagger}{\sqrt{2}}. \quad (6)
$$

Here, Ω (which is assumed to be real) denotes the strength of the drive. Equation (6) contains co- and counter-rotating terms. Neglecting the counter-rotating terms, the drive within the rotating wave approximation (RWA) simplifies to

$$
(\hat{V}_{\text{drive}})_{\text{RWA}} = \frac{\Omega}{2\iota\sqrt{2}}(e^{\iota\omega_D t}\hat{a} - e^{-\iota\omega_D t}\hat{a}^\dagger). \quad (7)
$$

Looking ahead, we define the detuning Δ between the external drive and the natural angular frequency of the harmonic oscillator Hamiltonian $\hat{H}_0$ (in our case, this angular frequency is equal to 1),

$$
\Delta = \omega_D - 1. \quad (8)
$$

The master equation, Eq. (1), contains five dissipators $\hat{\mathcal{D}}$, which—for an arbitrary operator $\hat{C}$—are defined through

$$
\hat{\mathcal{D}}[\hat{C}](\hat{\rho}) = \hat{C}\hat{\rho}\hat{C}^\dagger - \frac{1}{2}\{\hat{C}^\dagger\hat{C}, \hat{\rho}\}, \quad (9)
$$

where $\{\hat{A}, \hat{B}\}$ denotes the anticommutator between the operators $\hat{A}$ and $\hat{B}$. The dissipators that are proportional to the coefficients γ_1^+ and γ_1^- represent incoherent linear or one-excitation processes while those that are proportional to α, β, and δ represent incoherent nonlinear or two-excitation processes. Specifically, γ_1^+ and γ_1^- are incoherent linear gain and incoherent linear damping rates, respectively. The dissipator proportional to the incoherent two-photon damping coefficient α appears in various contexts including phonon lasers and lasing [23,28,29]. The terms that are proportional to β and δ, in contrast, are studied comparatively rarely [7,8]. The physical interpretation of these terms is relegated to Sec. II B, which connects the quantum equations of motion to the classical equations of motion for the generalized RvdP oscillator.

In the eigenbasis $\{|k\rangle\}$ of $\hat{H}_0$, the master equation reads

$$\dot{\rho}_{k,l} = -\iota \frac{\Omega}{\sqrt{2}} \sin(\omega_D t)(\sqrt{k}\rho_{k-1,l} + \sqrt{k+1}\rho_{k+1,l} - \sqrt{l+1}\rho_{k,l+1} - \sqrt{l}\rho_{k,l-1})$$

$$+ \left[-\iota(k-l) - \frac{\gamma_1^+}{2}(k+l+2) - \frac{\gamma_1^-}{2}(k+l) - \frac{\alpha}{2}[k(k-1)+l(l-1)] + \left(\frac{\beta}{4}+\frac{\delta}{4}\right)(2kl - 2k^2 - 2l^2 + k + l)\right]\rho_{k,l}$$

$$+ \gamma_1^+ \sqrt{kl}\rho_{k-1,l-1} + \gamma_1^- \sqrt{(k+1)(l+1)}\rho_{k+1,l+1} + \left(\alpha + \frac{\beta}{2} + \frac{\delta}{2}\right)\sqrt{(k+1)(k+2)(l+1)(l+2)}\rho_{k+2,l+2}$$

$$+ \frac{1}{4}(\beta - \delta)[(2l-k)\sqrt{(k+1)(k+2)}\rho_{k+2,l} + (2k-l)\sqrt{(l+1)(l+2)}\rho_{k,l+2}$$

$$+ (2-l)\sqrt{l(l-1)}\rho_{k,l-2} + (2-k)\sqrt{k(k-1)}\rho_{k-2,l}], \tag{10}$$

where we introduced the notation $\rho_{k,l} = \langle k|\hat{\rho}|l\rangle$ and $\dot{\rho}_{k,l} = \langle k|\dot{\hat{\rho}}|l\rangle$. To understand the system dynamics, it is useful to summarize the structure of the coupled differential equations. For $\Omega = 0$, Eq. (10) shows the following:

(i) $\beta = \delta$ [30]: The coupled differential equations for $\dot{\rho}_{k,l}$ decouple into N independent sets of equations; specifically, the equation for $\dot{\rho}_{0,0}$ is only coupled to the equations for $\dot{\rho}_{n,n}$, where $n = 1, \ldots, N-1$; the equation for $\dot{\rho}_{0,1}$ is only coupled to the equations for $\dot{\rho}_{n,n+1}$, where $n = 1, \ldots, N-2$; and so on. Since the coherences can be shown to decay to zero in the large time limit, the stationary $\Omega = 0$ limit cycle state is characterized by $\rho_{k,l} = 0$ for $k \neq l$, i.e., it is diagonal in the energy eigenbasis of $\hat{H}_0$. Reference [28] provides analytical expressions for the $\rho_{k,k}$ that characterize the limit cycle. A diagonal density matrix yields a rotationally invariant Wigner function $W(x, p, t)$ (see, e.g., Refs. [8,27]), i.e., a Wigner function that depends on r but not on φ; here, $x = r\cos\varphi$ and $p = r\sin\varphi$.

(ii) $\beta \neq \delta$: The coupled differential equations for the $\dot{\rho}_{k,l}$ can be divided into two sets, one set for $\dot{\rho}_{k,l}$ with $k - l$ even and another set for $\dot{\rho}_{k,l}$ with $k - l$ odd. The stationary $\Omega = 0$ limit cycle state is characterized by $\rho_{k,l} = 0$ for all odd $k - l$. Owing to the dissipators that are proportional to β and δ, the limit cycle state is nondiagonal in the energy eigenbasis of $\hat{H}_0$. Correspondingly, the Wigner function depends explicitly on r and φ.

The drive (i.e., a finite Ω) introduces coupling between $\dot{\rho}_{k,l}$ equations with $k - l$ even and $k - l$ odd. Specifically, in the weak driving limit, a perturbative order-by-order treatment (using the framework discussed in Ref. [20]) shows that the drive introduces terms that are proportional to Ω in the off diagonals $\rho_{k,k\pm1}$ when $\beta = \delta$ and in the elements $\rho_{k,l}$ with $k - l$ odd when $\beta \neq \delta$.

Throughout, we are interested in parameter combinations for which the density matrix at large times reaches a state that displays regular oscillations around a quasistationary state. Our simulations prepare the system at $t = 0$ in the coherent state $|\alpha_0\rangle$ [31]. The time evolution of the matrix elements $\rho_{k,l}$ is determined by solving the set of first-order coupled differential equations given by Eq. (10).

We visualize the system at time t using the phase space Wigner function $W(x, p, t)$,

$$W(x, p, t) = \frac{1}{\pi} \int_{-\infty}^{\infty} \langle x+y|\hat{\rho}|x-y\rangle e^{-2\iota py} dy, \tag{11}$$

which is a quasiprobability [31]. A key feature of the Wigner function is that it connects naturally with the classical phase space trajectories of the corresponding classical system.

B. Connection with classical equation of motion

Starting with the equation of motion for $\langle \hat{a} \rangle$,

$$\frac{d\langle \hat{a} \rangle}{dt} = \text{Tr}(\dot{\hat{\rho}}\hat{a}), \tag{12}$$

our goal is to obtain an approximate differential equation for $\langle \hat{x} \rangle$ that maps—in the limit that ϵ,

$$\epsilon = \gamma_1^+ - \gamma_1^-, \tag{13}$$

is small—to the classical equations of motion for the generalized driven RvdP oscillator. Positive and negative ϵ correspond to net linear gain and net linear damping, respectively. Importantly, when establishing the mapping between the quantum and classical equations of motions, only the difference between γ_1^+ and γ_1^- enters and not the actual values [8]. In the quantum regime, the system characteristics have, however, been shown to depend on the actual values of γ_1^+ and γ_1^- [8]. Expectation values are, as usual, calculated via the trace operation; e.g., $\langle \hat{a} \rangle = \text{Tr}(\hat{\rho}\hat{a})$. Introducing $\bar{\alpha} = \alpha/\epsilon$, $\bar{\beta} = \beta/\epsilon$, $\bar{\delta} = \delta/\epsilon$, and $\bar{\Omega} = \Omega/\epsilon$ as well as replacing terms like $\langle \hat{a}^\dagger \hat{a}\hat{a} \rangle$ by $\langle \hat{a}^\dagger \rangle \langle \hat{a} \rangle \langle \hat{a} \rangle$, one derives—generalizing the steps of Arosh et al. [8]—at order ϵ

$$\frac{d^2\langle \hat{x} \rangle}{dt^2} + \langle \hat{x} \rangle = -\epsilon\bar{\Omega}\sin(\omega_D t) + \epsilon\left[1 - (\bar{\alpha} + 2\bar{\beta}\right.$$

$$\left. - \bar{\delta})\langle \hat{x} \rangle^2 - (\bar{\alpha} + \bar{\delta})\left(\frac{d\langle \hat{x} \rangle}{dt}\right)^2\right]\frac{d\langle \hat{x} \rangle}{dt}. \tag{14}$$

Physically, the approximations amount to assuming that the classical limit cycle is only weakly deformed and that quantum fluctuations are small. The quantum-classical
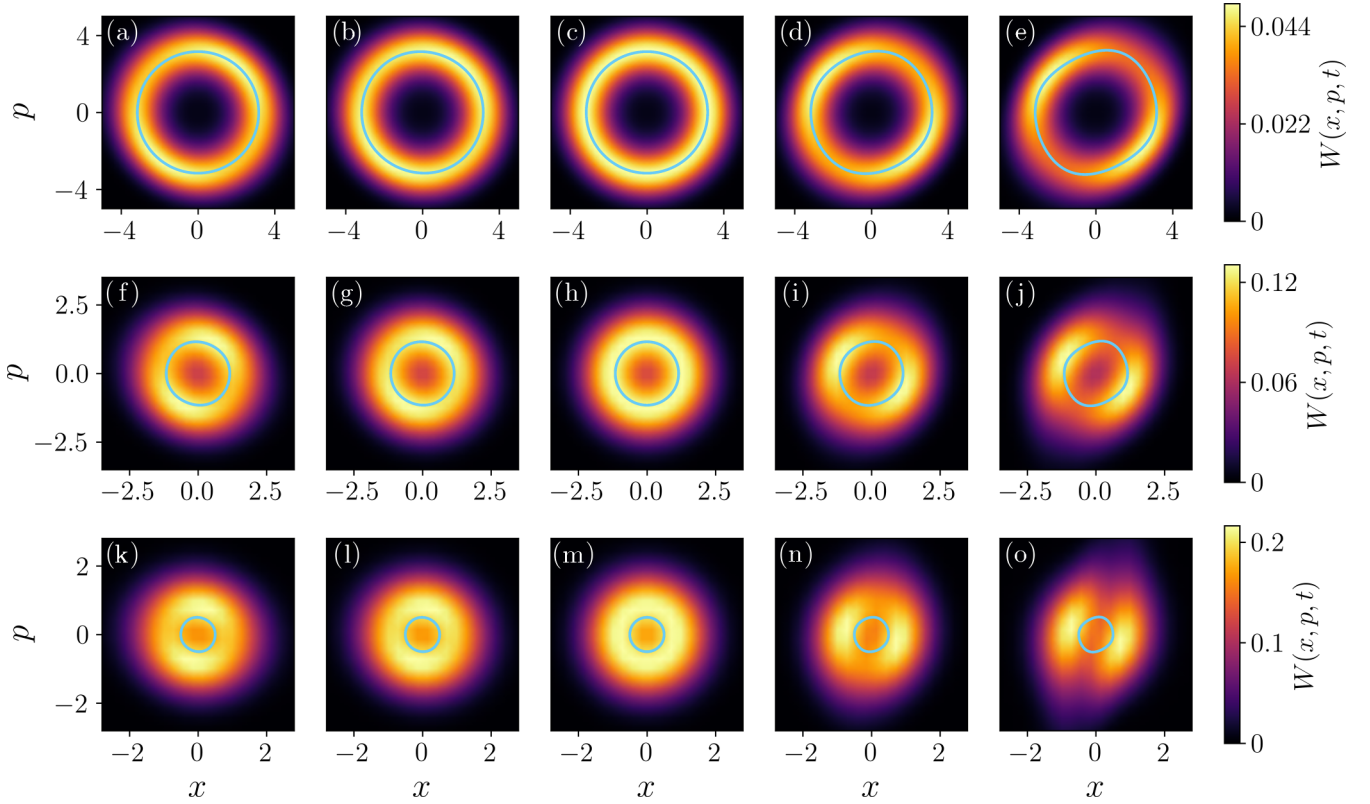
FIG. 1. Stationary quantum Wigner functions $W(x, p, t)$ [Eq. (11)] as functions of x and p in the absence of an external drive; the calculations are performed in the laboratory frame using Eq. (10) with $\Omega = 0$. The linear gain rate γ_1^+ and linear damping rate γ_1^- are equal to 1/5 and 0, respectively, yielding $\epsilon = 1/5$; note, to amplify the rotational asymmetry, this value of ϵ is twice as large as that used in all other figures of this paper. The nonlinear damping parameters as well as the values of $\langle \hat{a}^\dagger \hat{a} \rangle$ and $A_{\rm lc}$ ($A_{\rm lc}$ is the same for all five panels in a given row) can be found in Table I. From top to bottom, the quantumness, as measured by $\langle \hat{a}^\dagger \hat{a} \rangle$, decreases; specifically, $\langle \hat{a}^\dagger \hat{a} \rangle$ is 5.5–5.6, 1.18–1.34, and 0.53–0.83 for the first, second, and third row, respectively. The color scales on the far right apply to all five distributions in the respective row. Note that the scales of the axes are the same for all panels in a given row but that the x and p ranges decrease from the first to the second and from the second to the third rows. The first, third, and fifth columns are for the R, RvdP, and vdP oscillators, respectively. The second column is for an oscillator that is "in between" the R and Rvdp oscillators while the fourth column is for an oscillator that is "in between" the RvdP and vdP oscillators. The light blue solid lines show the classical limit cycle trajectory.

correspondence for the strongly non-linear regime (lifting of the former restriction) can be established by allowing for additional terms in $\hat{H}_0$. Reference [7] carried such a program out for the R, RvdP, and vdP oscillators.

Defining $\bar{\gamma}_{2,\rm vdp} = \bar{\alpha} + 2\bar{\beta} - \bar{\delta}$ and $\bar{\gamma}_{2,\rm ray} = \bar{\alpha} + \bar{\delta}$ and replacing the expectation value $\langle \hat{x} \rangle$ by the classical variable $x(t)$, Eq. (14) can be identified as the classical equation of motion for a driven self-sustained oscillator:

$$\ddot{x}(t) + x(t) = -\epsilon \bar{\Omega} \sin[(1 + \Delta)t]$$
$$+ \epsilon [1 - \bar{\gamma}_{2,\rm vdp}(x(t))^2 - \bar{\gamma}_{2,\rm ray}(\dot{x}(t))^2]\dot{x}(t). \tag{15}$$

The subscript "2" reflects that $\bar{\gamma}_{2,\rm vdp}$ and $\bar{\gamma}_{2,\rm ray}$ characterize nonlinear damping processes; throughout, these coefficients are assumed to be greater than or equal to zero. The subscripts "vdp" and "ray" stand for "van der Pol" and "Rayleigh," respectively. The combinations $(\bar{\gamma}_{2,\rm vdp} > 0, \bar{\gamma}_{2,\rm ray} = 0)$ and $(\bar{\gamma}_{2,\rm vdp} = 0, \bar{\gamma}_{2,\rm ray} > 0)$ correspond to the paradigmatic vdP and R oscillators [7,8]. The case where the damping rates $\bar{\gamma}_{2,\rm vdp}$ and $\bar{\gamma}_{2,\rm ray}$ are equal is referred to as the RvdP oscillator [7,8]. In terms of $\bar{\alpha}$, $\bar{\beta}$, and $\bar{\gamma}$, the three special cases are

vdP oscillator with $\bar{\alpha} = -\bar{\delta}$, RvdP oscillator with $\bar{\beta} = \bar{\delta}$, and R oscillator with $\bar{\alpha} + 2\bar{\beta} = \bar{\delta}$. By changing $\bar{\gamma}_{2,\rm vdp}$ and $\bar{\gamma}_{2,\rm ray}$ continuously one can tune from one oscillator type to another.

The classical equations of motion can be analyzed using secular perturbation theory, in which ϵ is treated— consistently with the discussion above—as a small parameter [32,33]. Defining the scaled detuning $\bar{\Delta}$ as well as the slow timescale T [$\bar{\Delta} = \Delta/\epsilon$ and $T = \epsilon t$; since T depends on t, we use the notation $T(t)$], one makes the ansatz

$$x(t) = \tfrac{1}{2}A(T(t))\exp(\iota t) + \tfrac{1}{2}[A(T(t))]^* \exp(-\iota t) + \epsilon x_1(t), \tag{16}$$

where the amplitude A is assumed to be a slowly varying function in T. In the absence of an external drive, the amplitude $|A(T(t))| = A_{\rm lc}$,

$$A_{\rm lc} = 2(\bar{\gamma}_{2,\rm vdp} + 3\bar{\gamma}_{2,\rm ray})^{-1/2}, \tag{17}$$

corresponds to a stable limit cycle (hence the subscript "lc"). Regardless of where the classical trajectory is started, it approaches at long times a trajectory that is, to leading order, characterized by $A_{\rm lc}$ [1,32]. The solid light blue lines in Fig. 1

TABLE I. The first six columns provide a summary of nonlinear damping parameters α, β, and δ used in Figs. 1, 4–6; the labels (a)–(o) refer to the panels of the figures. For reference, the last two columns report the limit cycle amplitude A_{lc}, which depends on the parameter ϵ; $\epsilon = 1/5$ and $1/10$ for Fig. 1 and Figs. 4–6, respectively. In each figure, the classical limit cycle amplitude A_{lc} is the same across each row [e.g., panels (a)–(e)]. The labels "classical," "transition," and "quantum" refer to the quantumness of the system; the labels are meant to serve as a rough guide.

		R		R/RvdP		RvdP		RvdP/vdP		vdP	A_{lc} for Fig. 1	A_{lc} for Figs. 4–6
α	(a)	0	(b)	1/100	(c)	1/50	(d)	1/100	(e)	0	"classical"	"classical"
β		1/75		1/150		0		1/50		1/25	$A_{lc} = \sqrt{10}$	$A_{lc} = \sqrt{5}$
δ		2/75		1/75		0		0		0	≈ 3.162	≈ 2.236
α	(f)	0	(g)	3/40	(h)	3/20	(i)	3/40	(j)	0	"transition"	"transition"
β		1/10		1/20		0		3/20		3/10	$A_{lc} = \sqrt{4/3}$	$A_{lc} = \sqrt{2/3}$
δ		1/5		1/10		0		0		0	≈ 1.155	≈ 0.816
α	(k)	0	(l)	2/5	(m)	4/5	(n)	2/5	(o)	0	"quantum"	"quantum"
β		8/15		4/15		0		4/5		8/5	$A_{lc} = 1/2$	$A_{lc} = \sqrt{1/8}$
δ		16/15		8/15		0		0		0	$= 0.5$	≈ 0.354

show the numerically determined classical limit cycle trajectories for $\Omega = 0$ and $\epsilon = 1/5$ for various oscillator types and various nonlinear parameters, i.e., various A_{lc} values. The limit cycle is a prerequisite for the emergence of classical synchronization in the presence of a nonvanishing drive with Ω and $|\Delta|$ not too large [1]. One objective of the present work is to study the quantum analog of the celebrated classical Arnold tongues, which play a fundamental role in synchronization studies, for the generalized RvdP oscillator with rotational phase space asymmetry.

The mapping between the classical and quantum equations of motion motivates the functional forms of the "nonlinear dissipators." Specifically, the arguments of the dissipators that are proportional to β and δ are chosen such that the quantum equations of motion map, for small ϵ, to the classical equations of motion for the R and vdP oscillators. While the dissipator $\hat{\mathcal{D}}[\hat{a}^2](\hat{\rho})$ has a clear physical interpretation (two-photon losses), it was suggested that an experimental realization of the dissipators $\hat{\mathcal{D}}[\hat{x}\hat{a}](\hat{\rho})$ and $\hat{\mathcal{D}}[\hat{p}\hat{a}](\hat{\rho})$ may involve measurement and feedback processes [7].

We emphasize that the mapping between the classical and quantum equations of motion is derived in the laboratory frame. This is important since the terms $\hat{\mathcal{D}}[\hat{x}\hat{a}](\hat{\rho})$ and $\hat{\mathcal{D}}[\hat{p}\hat{a}](\hat{\rho})$ are not invariant under a transformation to a rotating frame (see Appendix A), i.e., the functional form of the master equation changes unless β and δ are equal to each other. The terms $\hat{\mathcal{D}}[\hat{a}^\dagger](\hat{\rho})$, $\hat{\mathcal{D}}[\hat{a}](\hat{\rho})$, and $\hat{\mathcal{D}}[\hat{a}\hat{a}](\hat{\rho})$, in contrast, are unchanged under a transformation to a rotating frame. It follows that only the master equation for the RvdP oscillator is invariant under a transformation to a rotating frame. In general, a transformation to a rotating frame introduces new terms, which can be interpreted as being due to fictitious forces that arise in response to the rotation, in analogy to, e.g., the Coriolis force in classical mechanics [34].

C. Observables

As alluded to earlier, the expectation value $\langle\hat{a}^\dagger\hat{a}\rangle$ measures the quantumness of the oscillator. The self-sustained oscillator is, in the absence of the external drive, in the classical regime, the crossover regime, and the quantum regime when $\langle\hat{a}^\dagger\hat{a}\rangle \gg 1$, $\langle\hat{a}^\dagger\hat{a}\rangle \approx 1$, and $\langle\hat{a}^\dagger\hat{a}\rangle \ll 1$, respectively. Being in the quantum regime requires that the dissipators that lead to a lowering of the excitations are sufficiently strong. For the RvdP oscillator with $\beta = \delta$, e.g., the effects of the α and γ_1^- terms need to dominate over the γ_1^+ term. A nonvanishing external drive tends to act as an energy source, leading to an increase of $\langle\hat{a}^\dagger\hat{a}\rangle$ in the quasistationary regime compared to the situation where the drive strength is zero. Quite generally, the system dynamics can be divided into two regimes: initial transient dynamics and long-time quasistationary dynamics. Figures 2 and 3 show the time dependence of observables, covering the transient and quasistationary regimes, while Figs. 1, 4–6 display the system characteristics in the quasistationary regime, which—for the parameters considered—is governed, at least to leading order, by the limit cycle of the system without external drive.

Our primary interest in this work lies in quantifying phase localization and frequency entrainment, in the nontransient quasistationary regime. Quantum phase localization has been quantified through various measures, including phase distribution, "moments" such as $\langle\hat{a}\rangle$, entanglement, and information theory based observables [13,17,22,25,35,36]. Measures that involve the quantum mechanical phase operator $\hat{\varphi}$ [37,38] are intuitively appealing as they provide an immediate link to one of the classical phase localization metrics, namely the mean resultant length S_{cl}, which is defined as $S_{cl} = \sqrt{\langle\sin\varphi\rangle^2 + \langle\cos\varphi\rangle^2} = |\langle\exp(\iota\varphi)\rangle|$. In this classical context, the $\langle\cdot\rangle$ notation indicates an ensemble average as opposed to the quantum mechanical trace operation. If the phases φ, $\varphi = \operatorname{atan}(p/x)$, for the driven self-sustained classical oscillator are distributed uniformly, S_{cl} is equal to zero. For nonuniformly distributed φ, on the other hand, S_{cl} is finite but never larger than 1. By analogy, quantum phase localization is quantified through (see, e.g., Ref. [21])

$$S_q = |\langle\exp(\iota\hat{\varphi})\rangle|. \tag{18}$$

It follows straightforwardly that S_q lies between 0 and 1, just like the classical mean resultant length S_{cl}. A value of $S_q = 0$ indicates the absence of phase localization while a value of 1 indicates maximal phase localization.
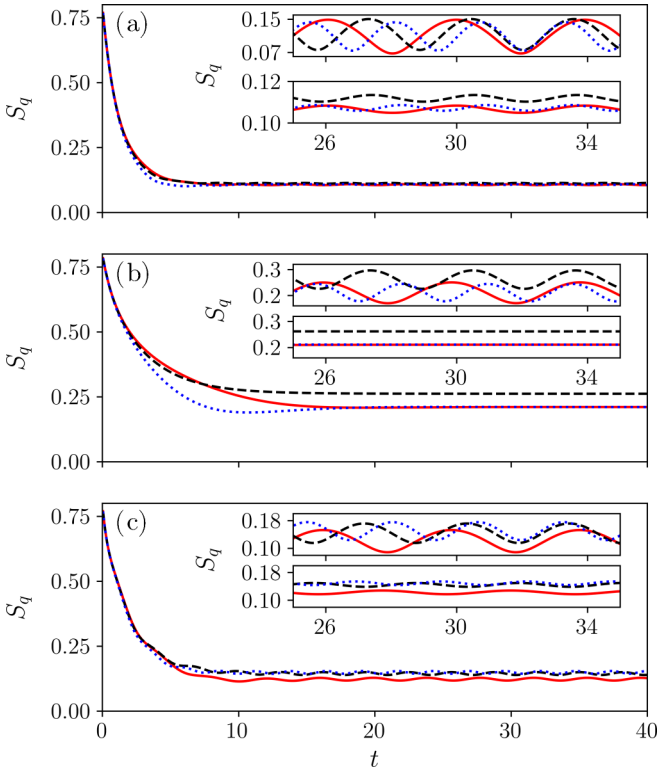
FIG. 2. Phase localization S_q, calculated in the laboratory frame, as a function of time for (a) the R oscillator [$\alpha = 0$, $\beta = 8/15$, and $\delta = 16/15$; same nonlinear parameters as used in Figs. 1(k), 3(k), 5(k), and 6(k)], (b) the RvdP oscillator [$\alpha = 4/5$, $\beta = 0$, and $\delta = 0$; same nonlinear parameters as used in Figs. 1(m), 3(m), 5(m), and 6(m)], and (c) the vdP oscillator [$\alpha = 0$, $\beta = 8/5$, and $\delta = 0$; same nonlinear parameters as used in Figs. 1(o), 3(o), 5(o), and 6(o)] with linear parameters $\gamma_1^+ = 1/5$ and $\gamma_1^- = 1/10$ in the presence of an external drive with $\Omega = 3/10$. The black dashed, red solid, and blue dotted lines are for $\Delta = 0$, $-1/5$, and $1/5$, respectively. The oscillators are, at $t = 0$, prepared in a coherent state with $x_0 = p_0 = 3/(2\sqrt{2}) \approx 1.061$. The results in the main figure employ the RWA. In the quasistationary long-time limit ($t \gtrsim 10$–20), the phase localization for the R and vdP oscillators display oscillations; these oscillations are enlarged in the lower inset in each of the panels. For comparison, the top inset in each of the panels shows the phase localization within the beyond-RWA (BWRA). Compared to the RWA, the BRWA terms introduce larger amplitude oscillations.

It is useful to rewrite S_q, Eq. (18), in terms of the density matrix elements (see Appendix B):

$$S_q = \left| \sum_{n=1}^{\infty} \rho_{n,n-1} \right|. \qquad (19)$$

This expression highlights that S_q is governed by the coherences of the density matrix. Using the properties discussed in the context of Eq. (10), it can be shown readily that S_q vanishes in the $\Omega = 0$ and $t \to \infty$ limits for all oscillator types considered in this work. Correspondingly, the nonvanishing values of S_q observed in this work are introduced by the external drive. If Ω is too large, the external drive may reshape the $\Omega = 0$ limit cycle so strongly that the oscillator's amplitude changes notably. To quantify amplitude distortions,
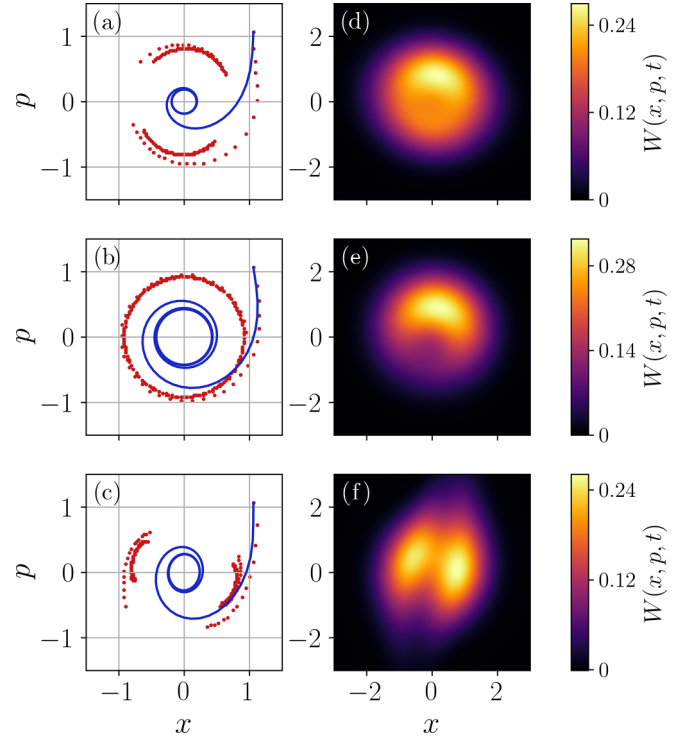

FIG. 3. Dynamics for $0 \leqslant t \lesssim 50$ (left column) and Wigner function at $t \approx 30$ (right column) in the laboratory frame, calculated within the RWA, for (a)/(d) the R oscillator, (b)/(e) the RvdP oscillator, and (c)/(f) the vdP oscillator in the presence of an external drive with $\Omega = 3/10$ and $\Delta = 0$. The linear and nonlinear parameters in (a)/(d), (b)/(e), and (c)/(f) are the same as in Figs. 2(a), 2(b), and 2(c), respectively. The blue line and red dots show the center-of-mass trajectory and the trajectory at which the Wigner function is maximal, respectively; the red dots are calculated at evenly spaced time intervals.

we compare the radius R at which the Wigner function takes its maximum for finite and vanishing drive strengths.

We note that while Ref. [20] states that a rotationally invariant limit cycle is a prerequisite for finite phase localization, we quantify phase localization also for $\Omega = 0$ limit cycles that possess broken rotational symmetry, i.e., for limit cycles that are characterized by nonzero $\rho_{k,l}$ elements for $|k - l| = 2, 4, \ldots$. Specifically, the next section investigates whether self-sustained oscillators with nonrotationally symmetric limit cycles (those with $\beta \neq \delta$ or, equivalently, $\gamma_{2,\text{vpd}} \neq \gamma_{2,\text{ray}}$) enhance or hinder quantum phase localization.

To quantify frequency entrainment, we calculate the power spectrum $S_p(\omega, \tau)$ [10],

$$S_p(\omega, \tau) = \int_{-\infty}^{\infty} C(t, \tau) \exp(-\imath \omega t) dt, \qquad (20)$$

which is defined as the Fourier transform of the correlation function $C(t, \tau)$,

$$C(t, \tau) = \langle \hat{a}^\dagger(t + \tau) \hat{a}(\tau) \rangle. \qquad (21)$$

The correlation function $C(t, \tau)$ is obtained by averaging over the full quantum mechanical density matrix (system and environment), making use of the regression theorem [39]. Since our main focus lies in characterizing the system behavior in
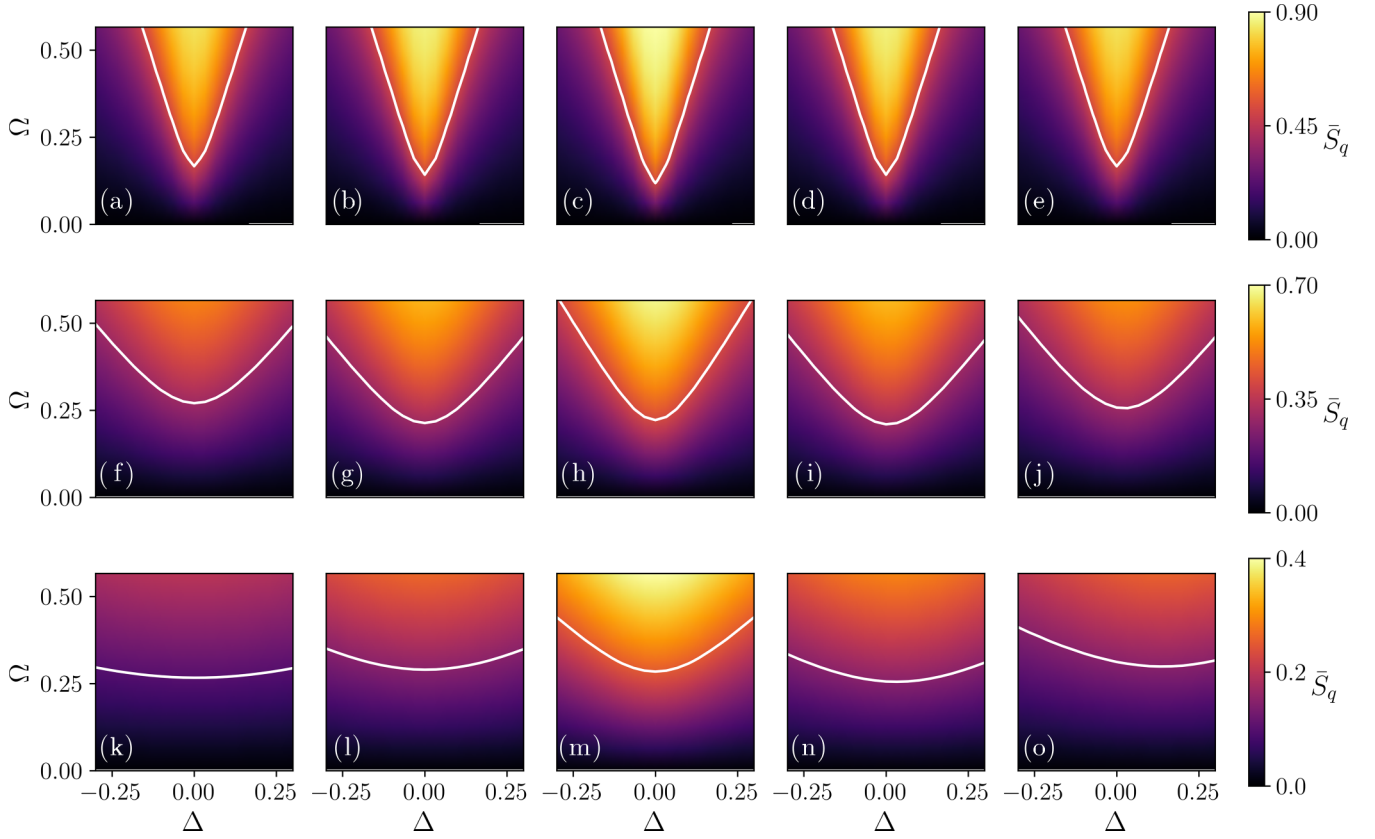
FIG. 4. Time-averaged phase localization $\bar{S}_q$ as functions of the detuning Δ and the drive strength Ω; the calculations are performed in the laboratory frame within the RWA. The linear gain coefficient γ_1^+ and linear damping coefficient γ_1^- are equal to $1/5$ and $1/10$, respectively, yielding $\epsilon = 1/10$ (this value is smaller than that used in Fig. 1). The nonlinear damping parameters as well as the values of A_{lc} (A_{lc} is the same for the five panels in a given row) can be found in Table I. As a guide to the eye, the white lines show lines of constant $\bar{S}_q$.

the nontransient quasistationary regime, we restrict ourselves to sufficiently large τ. To calculate $S_p(\omega, \tau)$, we work in the frame that rotates with the drive. As mentioned earlier and discussed formally in Appendix A, the transformation from the laboratory to the rotating frame changes the functional form of the dissipators that are proportional to β and γ. In particular, the dissipators in the rotating frame are, in general, time dependent. Correspondingly, $S_p(\omega, \tau)$ depends explicitly on τ. The power spectrum, calculated in the frame rotating at ω_D, is expected to exhibit a delta-function-like spike at $\omega = 0$ as well as a broader response, possibly with pronounced side peaks [10,24,40,41]. If the center of a broad, non-delta-function-like peak lies at $\omega = 0$ as opposed to at $\omega = \Delta$, the system is said to be entrained: the broad response that is associated with the dissipative terms is linked to the drive frequency as opposed to the natural harmonic oscillator frequency. Recall, since the frame is rotating with ω_D, a response at $\omega = 0$ and $\omega = \Delta$ corresponds to being locked to the drive frequency and to being locked to the natural oscillator frequency, respectively.

III. RESULTS

This section discusses our results. After presenting Wigner functions for the undriven reference system (Fig. 1), we consider the driven system. Figures 2–6 discuss the phase

localization measure S_q and related observables while Figs. 7–9 present power spectra and their analysis with a view toward determining the presence or absence of frequency entrainment. Since the system is, according to the definition employed in this work, synchronized if the phase localization measure S_q is finite and if frequency entrainment is present, Figs. 2–4 and Figs. 7–9 are needed to fully characterize and understand synchronization, or absence thereof, in the systems under study.

Figure 1 shows snapshots of quasistationary Wigner functions for the undriven generalized RvdP oscillator in the laboratory frame. Three regimes are covered: the quantum regime characterized by $\langle \hat{a}^\dagger \hat{a} \rangle < 1$ (third row), the intermediate regime characterized by $\langle \hat{a}^\dagger \hat{a} \rangle \approx 1$ (second row), and the classical regime characterized by $\langle \hat{a}^\dagger \hat{a} \rangle > 1$ (first row). In the classical regime, the Wigner function takes on its (local) maxima at (x, p) values that closely follow the corresponding classical limit cycle trajectory (light blue solid line). The close resemblance between the (local) maxima of the quantum mechanical Wigner function $W(x, p, t)$ and the classical limit cycle trajectory in the classical regime confirms the quantum-classical correspondence derived in Sec. II B for the generalized RvdP oscillator in the small ϵ regime (Fig. 1 employs $\epsilon = 1/5$), thereby extending the work by Arosh *et al.* [8] for the R, RvdP, and vdP oscillators to include oscillators that lie between the R and RvdP oscillators (column 2 of
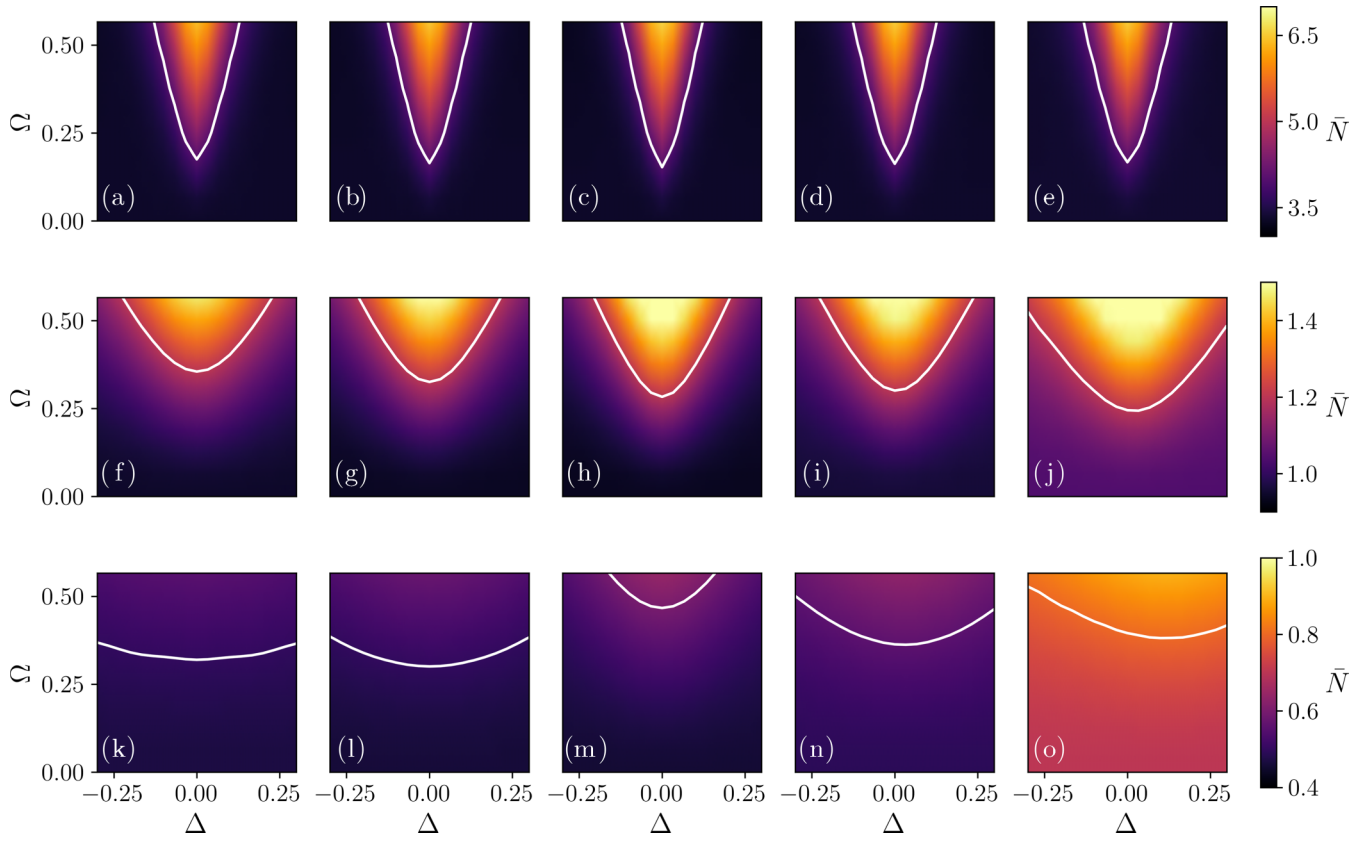
FIG. 5. Time-averaged number $\bar{N}$ of excitations as functions of the detuning Δ and the drive strength Ω; the calculations are performed in the laboratory frame within the RWA. The parameters are the same as those used in Fig. 4.
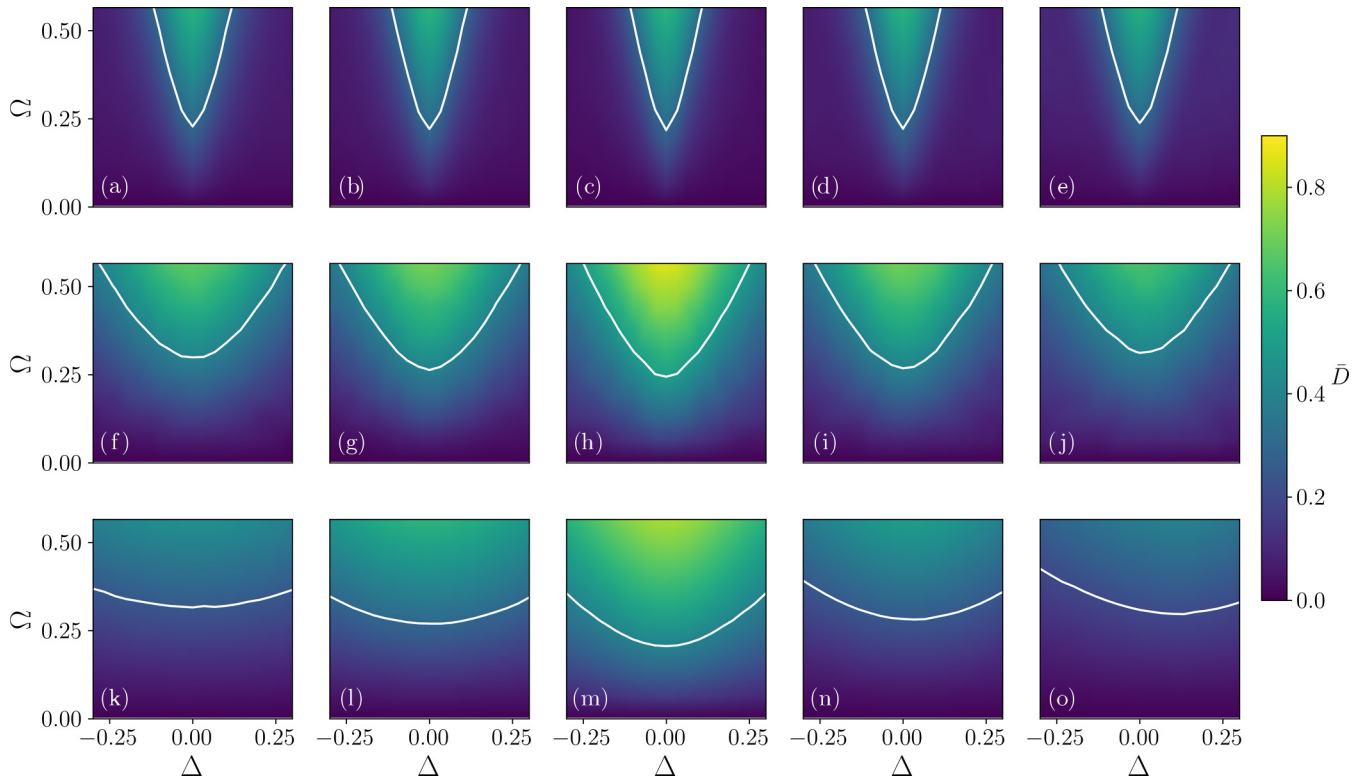

FIG. 6. Time-averaged deformation $\bar{D}$ as functions of the detuning Δ and the drive strength Ω; the calculations are performed in the laboratory frame within the RWA. The parameters are the same as those used in Figs. 4 and 5.
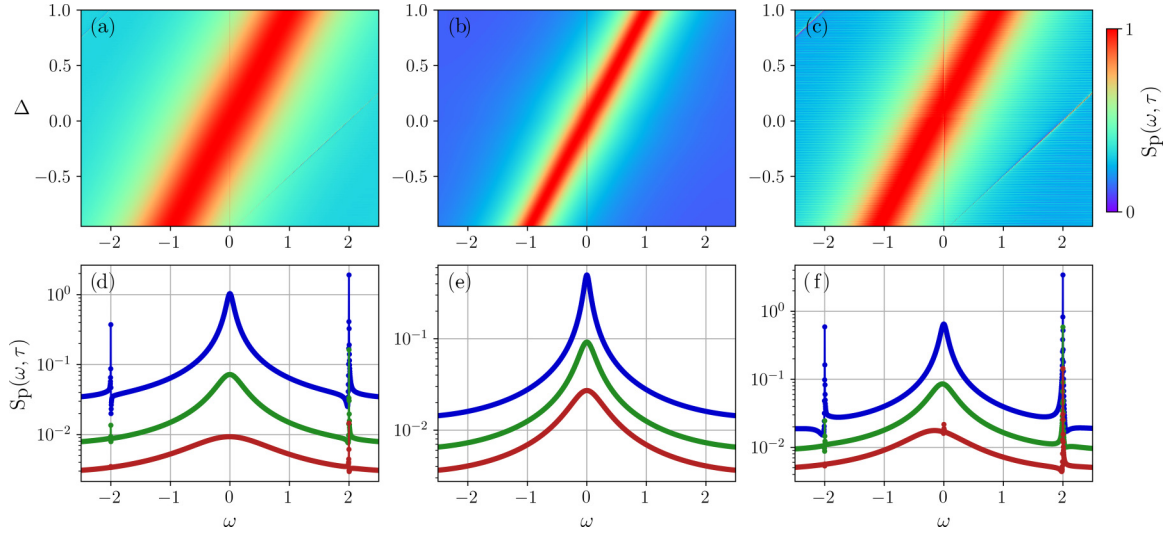
FIG. 7. The left, middle, and right columns show power spectra $S_p(\omega, \tau)$ for the R, RvdP, and vdP oscillators, respectively, for $\Omega = 3/10$, $\gamma_1^+ = 1/5$, $\gamma_1^- = 1/10$, and $\tau = 200$; the calculations are performed within the RWA in the frame that rotates at the drive frequency. Top row: Power spectra in the quantum regime as functions of ω and Δ. The non-linear damping parameters for panels (a), (b), and (c) are given in Table I(k), I(m), and I(o), respectively. For each Δ, the power spectrum is normalized to the maximum of the broad peak that is located at $\omega \approx \Delta$. The color bar on the right applies to all three spectra. Bottom row: Power spectra for $\Delta = 0$ as a function of ω. The red spectra (bottom curves) are $\Delta = 0$ cuts through the data shown in the top row. For comparison, the green (middle) and blue (top) curves show power spectra for the transition and classical regimes, respectively. The sharp δ-function-like data point at $\omega = 0$ is not shown and the data are not normalized. Note the logarithmic scale of the y axis. For panels (d)/(e)/(f), the nonlinear parameters for the spectra plotted in red (bottom curve), green (middle curve), and blue (top curve) are given in Table I(k)/I(m)/I(o), I(f)/I(h)/I(j), and I(a)/I(c)/I(e), respectively.
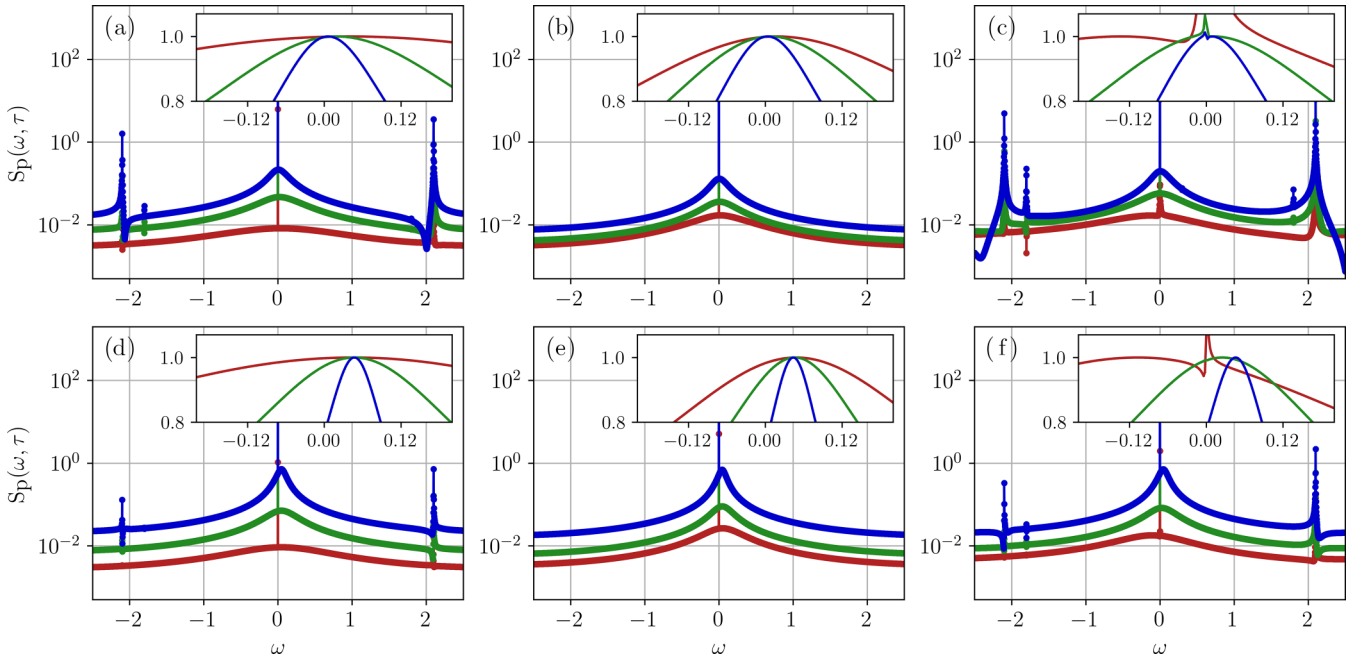

FIG. 8. The left, middle, and right columns show power spectra $S_p(\omega, \tau)$ for the R, RvdP, and vdP oscillators, respectively, for $\Delta = 1/20$, $\gamma_1^+ = 1/5$, $\gamma_1^- = 1/10$, and $\tau = 200$; the calculations are performed within the RWA in the frame that rotates at the drive frequency. Top row: Power spectra for $\Omega = 3\sqrt{2}/5$. Bottom row: Power spectra for $\Omega = \sqrt{2}/5$. For panels (a)&(d)/(b)&(e)/(c)&(f), the non-linear parameters for the spectra plotted in red (bottom curve), green (middle curve), and blue (top curve) are given in Table I(k)/I(m)/I(o), I(f)/I(h)/I(j), and I(a)/I(c)/I(e), respectively. The insets show blow-ups of the region around $\omega = 0$; in these plots, the normalization is chosen such that the maximum of the broad peak is equal to 1 and the δ-function-like spike is removed.

Fig. 1) or between the RvdP and vdP oscillators (column 4 of Fig. 1). We also checked that classical finite-temperature ensemble calculations, in which the temperature mimics the role of the quantum fluctuations, reproduces the Wigner functions semi-quantitatively for all oscillator types considered. This observation further confirms the limiting classical behavior derived in Sec. II B.

The quasistationary Wigner functions for the RvdP oscillator without external drive (column 3 of Fig. 1) are, as discussed in Sec. II B, rotationally symmetric in all regimes (quantum to classical). For the corresponding classical system, the nonlinear damping term (i.e., the term that is proportional to $x^2 + \dot{x}^2$) is directly proportional to the energy and thus constant along the circular trajectory (solid light blue lines). As α increases from Fig. 1(c) to Fig. 1(h) to Fig. 1(m), the nonlinear damping becomes stronger, $\langle \hat{a}^\dagger \hat{a} \rangle$ decreases, and the ring-shaped Wigner function "shrinks."

The classical limit cycle trajectories for the other oscillator types (columns 1, 2, 4, and 5 of Fig. 1) are not circular but slightly deformed, reflecting the fact that the nonlinear damping terms $x^2 \dot{x}$ and $\dot{x}^3$ contribute with unequal strengths. For the vdP oscillator, e.g., the classical trajectory reaches its most positive and most negative p values at finite positive and finite negative x values, respectively (column 5 of Fig. 1). Since the magnitude of the velocity is largest at these points, the system spends less time in these phase space regions than in other phase space regions. Interestingly, these classical features are inherited by the quasistationary Wigner function, which displays two global maxima that are, roughly, located at $p \approx -x \approx \pm 3$ for the largest $\langle \hat{a}^\dagger \hat{a} \rangle$ considered. In the quantum regime, the Wigner function of the vdP oscillator is characterized by two "tilted lobes." While the classical limit cycle trajectory does not capture the detailed structure of the Wigner function, it can be used to estimate the "tilt angle" and location of the lobe maxima. The R oscillator (column 1 of Fig. 1) possesses, like the vdP oscillator, a rotational phase-space asymmetry, with the roles of x and p being reversed in the nonlinear damping term. As a consequence, the tilt angle of the R oscillator differs in the quantum regime by about $\pi/2$ from that of the vdP oscillator [see Fig. 1(k)].

The quasistationary Wigner functions, i.e., the quantum mechanical limit cycles, are critical for observing phase synchronization in the presence of an external drive. Working within the RWA, we consider the regime where the drive is perturbative in the sense that the drive does not destroy the limit cycle that is supported by the system with vanishing drive; this aspect is discussed in more detail below in the context of Fig. 6. Figures 2(a), 2(b), and 2(c) show the phase localization S_q, calculated in the laboratory frame, as a function of time for the R, RvdP, and vdP oscillators for damping and gain parameters that, in the absence of the external drive, fall into the quantum regime. Since the initial state is a coherent state with relatively well defined phase, the phase localization decreases approximately monotonically during the transient dynamics ($t \lesssim 10$ in Fig. 2) during which the Wigner function moves toward the limit cycle. For $t \gtrsim 10$ or 20, the phase localization is essentially constant [Fig. 2(b)] or displays regular oscillatory behavior [Figs. 2(a) and 2(c)]. Figure 4 includes the transient dynamics to show the order of magnitude of the time that is needed to reach the

quasistationary regime. Throughout, we are interested in physics that is independent of the initial state. Because of this we should, strictly speaking, refer to the quantity S_q as phase localization only in the quasistationary regime ($t \gtrsim 10$–20) and not in the transient regime (recall phase localization is a necessary but not sufficient condition for phase synchronization).

The black dashed, red solid, and blue dotted lines in Fig. 2 are for $\Delta = 0$, $-1/5$, and $1/5$, respectively. For the RvdP oscillator [see Fig. 2(b)], S_q is, in the large time limit, constant [this can be seen in the lower inset of Fig. 2(b), which shows a blow-up at large times]. For the same drive strength, S_q is larger for zero detuning than for finite detuning. This might be expected naively, as a finite detuning decreases the "similarity" of the system and the external drive, thereby hindering phase localization. In the transient regime, in contrast, S_q for the RvdP oscillator depends on the sign of the detuning Δ. The inclusion of the counter-rotating terms in the external coherent drive leads, as shown in the upper inset of Fig. 2(b), to oscillatory behavior of S_q in the long-time regime. It can be seen that the counter-rotating terms break the symmetry, i.e., the red solid and blue dotted lines (same $|\Delta|$ but opposite signs) are characterized by different oscillation periods (the oscillation frequency is equal to $2\omega_D$) as well as slightly different amplitudes. As expected for the relatively weak drive strength and small, in magnitude, detuning considered, the counter-rotating terms introduce relatively small corrections. Correspondingly, the results presented in Figs. 2–8 of this paper are obtained within the RWA.

Figure 3(e) shows a snapshot of the Wigner function at $t \approx 30$ for $\Delta = 0$ [the other parameters are the same as in Fig. 2(b)]. Since Ω is finite, the Wigner function is not rotationally symmetric but instead displays a half-moon shape. While the shape of $W(x, p, t)$ does not change appreciably for $t \gtrsim 10$, the entire distribution rotates with time. This can be seen from the blue line in Fig. 3(b), which shows the quantum mechanical ($\langle \hat{x} \rangle, \langle \hat{p} \rangle$)-trajectory as a function of time. In the quasi-stationary regime (i.e., the regime where the shape of the Wigner function does not change), the oscillation frequencies of $\langle \hat{x} \rangle$ and $\langle \hat{p} \rangle$ are regular and equal to ω_D (which is identical to that of the harmonic oscillator). For finite Δ (not shown), the oscillation frequencies of $\langle \hat{x} \rangle$ and $\langle \hat{p} \rangle$ for the RvdP oscillator are also equal to ω_D. The red dots in Fig. 3(b) show the ($\langle \hat{x} \rangle, \langle \hat{p} \rangle$)-values at which the Wigner function is maximal; to make the figure, the Wigner function is analyzed at about 300 equidistantly spaced times between 0 and 50. In the quasi-stationary regime, the red dots trace out a circle.

The phase localization for the R and vdP oscillators [Figs. 2(a) and 2(c)] decreases—similarly to that for the RvdP oscillator [Fig. 2(b)]—in the transient short-time regime. Key differences between the rotationally phase-space asymmetric and rotationally phase-space symmetric oscillators exist, however, in the quasi-stationary regime. For the R and vdP oscillators, S_q—calculated within the RWA—is oscillatory with oscillation period $T = \pi/\omega_D$ [see the main panels and lower insets of Figs. 2(a) and 2(c)]. As expected, inclusion of the counter-rotating terms enhances the oscillation amplitude [see the upper insets in Figs. 2(a) and 2(c)]. The main panels of Figs. 2(a) and 2(c) show that the phase localization for oscillator types that have rotationally asymmetric dissipators

depends in the quasi-stationary regime on the sign of the detuning, i.e., the phase localization displays an asymmetry with respect to $\Delta = 0$.

Figure 3 compares the dynamics for the R oscillator (top row) and the vdP oscillator (bottom row) for $\Delta = 0$ (same parameters as used in Fig. 2). While the ($\langle \hat{x} \rangle$, $\langle \hat{p} \rangle$)-trajectories (blue lines) follow a smooth path, the maximum of the Wigner function (red dots) changes rapidly over a short time interval, leading to a "bimodal" behavior that is not observed for the RvdP oscillator (see middle row of Fig. 3). A related bimodality was noted for an oscillator that contains squeezing-like operators [7]; more specifically, Ref. [7] included—to reproduce the classical R oscillator dynamics to higher order in ϵ—terms up to fourth-order in $\hat{a}$ and $\hat{a}^\dagger$ in the Hamiltonian and dissipators that are similar in form to our R oscillator. The fact that bi-modality is observed also in our case indicates that the rotational asymmetry of the dissipators, combined with a rotationally symmetric Hamiltonian, is sufficient for observing bimodality.

Since the radius R, $R = \sqrt{\langle \hat{x} \rangle^2 + \langle \hat{p} \rangle^2}$, at which the Wigner function is maximal is approximately constant for the undriven system in the quasi-stationary long-time regime, we use it to quantify the robustness of the limit cycle to the external drive. Specifically, we define the average deformation $\bar{D}$,

$$\bar{D} = \lim_{t_{\text{ref}} \to \infty} \frac{1}{T} \int_{t_{\text{ref}}}^{t_{\text{ref}}+T} \frac{|R_{\text{driven}}(t) - R_{\text{undriven}}|}{R_{\text{undriven}}} dt, \quad (22)$$

where t_{ref} is chosen such that the system dynamics is in the quasi-stationary regime, T denotes the oscillation period, and R_{undriven} and $R_{\text{driven}}(t)$ refer to the radii at which the Wigner distribution of the undriven ($\Omega = 0$) and driven ($\Omega \neq 0$) systems is maximal for identical parameters (except for Ω). While the radius $R_{\text{driven}}(t)$ of the driven system depends on time, the radius R_{undriven} of the undriven system is independent of time, provided t_{ref} is sufficiently large. A value of $\bar{D}$ close to zero signals that the drive has a perturbative effect on the amplitude of the limit cycle. The larger the value of $\bar{D}$ is, the more the amplitude of the limit cycle is modified by the external drive (the limit cycle might even get destroyed). Recall, the concept of phase synchronization assumes that the external drive localizes the phase while leaving the amplitude of the limit cycle approximately unchanged. For the parameters considered in Fig. 3, $\bar{D}$ is equal to 0.24 (top row), 0.52 (middle row), and 0.20 (bottom row). Interestingly, for the same drive strength Ω, the deformation $\bar{D}$ of the RvdP oscillator is larger than the deformation of the R and vdP oscillators (see also Fig. 6).

Figure 4 reports the time average $\bar{S}_q$,

$$\bar{S}_q = \lim_{t_{\text{ref}} \to \infty} \frac{1}{T} \int_{t_{\text{ref}}}^{t_{\text{ref}}+T} S_q(t) dt \quad (23)$$

[$S_q(t)$ is calculated within the RWA], as functions of Ω and Δ for 15 parameter combinations (the non-linear parameters are provided in Table I). Since $S_q(t)$ does not oscillate for the RvdP oscillator [see Fig. 2(b)], we set $\bar{S}_q = S_q$ in this case. The first, third, and fifth columns of Fig. 4 are for the R, RvdP, and vdP oscillators. The second and fourth columns are for oscillators that lie "in between" those featured in the

neighboring columns. The top, middle, and bottom rows are for parameters that fall, roughly, into the classical, transition, and quantum regimes.

Figure 4 shows that, for the drive strengths and detunings considered, the maximum of the phase localization $\bar{S}_q$ for each of the five oscillator types is larger in the classical regime than in the quantum regime. It is attributed to the fact that the extent or size of the Wigner functions decreases with decreasing $\langle \hat{a}^\dagger \hat{a} \rangle$ while the fluctuations (or "fuzziness") increases [10,17,42]. The average phase localization $\bar{S}_q$ for the RvdP oscillator (third column of Fig. 4) displays, in agreement with what was found previously [21], the celebrated Arnold tongue behavior. Specifically, the average phase localization $\bar{S}_q$ is symmetric with respect to $\Delta = 0$, increases (for the parameter combinations considered) with increasing Ω for fixed Δ, and generally decreases with increasing $|\Delta|$ for fixed Ω. Comparing Figs. 4(c), 4(h), and 4(m), it can be seen that the tongue becomes broader in the deep quantum regime, i.e., the relative change with $|\Delta|$ for fixed Ω is smaller in the deep quantum regime than in the classical regime.

Comparing the values of the time-averaged phase localization $\bar{S}_q$ for the different oscillator types with comparable $\langle \hat{a}^\dagger \hat{a} \rangle$, i.e., across rows, it can be seen that the maximum of the phase localization decreases as the dissipators that are not rotationally phase-space symmetric are turned on and play an increasingly important role. While the average phase localization $\bar{S}_q$ for the oscillators with rotationally phase-space asymmetric dissipators (first, second, fourth, and fifth columns in Fig. 4) behaves—in the classical and transition regime—rather similarly to that for the RvdP oscillator, clear differences are apparent in the deep quantum regime. Specifically, Figs. 4(k), 4(l), 4(n), and 4(o) reveal the following: (i) The average phase localization $\bar{S}_q$ is not symmetric with respect to $\Delta = 0$; (ii) starting at the Δ value for which $\bar{S}_q$ is minimal for a given Ω, $\bar{S}_q$ does not necessarily increase monotonically as one moves along the Δ axis; and (iii) for the parameters considered, $\bar{S}_q$ depends less strongly on Δ in Figs. 4(k), 4(l), 4(n), and 4(o) than in Fig. 4(m).

Figure 5 shows the time-averaged number $\bar{N}$ of excitations for the same 15 parameter combinations as those used in Fig. 4. Similar to $\bar{S}_q$, $\bar{N}$ is calculated by averaging $\langle \hat{a}^\dagger \hat{a} \rangle$ in the quasistationary regime over one time period. A visual comparison of $\bar{N}$ and $\bar{S}_q$ reveals a striking similarity of the two observables. While the black color represents different background values (zero in the case of $\bar{S}_q$ and a nonzero value in the case of $\bar{N}$), $\bar{S}_q$ and $\bar{N}$ appear to be changing in a correlated manner. Specifically, the time-averaged number $\bar{N}$ of excitations, plotted as functions of the detuning and drive strength, exhibits—in the classical and transition regimes—Arnold tongue-type characteristics. The fact that the observables $\bar{S}_q$ and $\bar{N}$ display similar characteristics, when visualized in terms of color plots as functions of Δ and Ω, may—at first sight—seem surprising as these two observables depend on different density matrix elements. As shown in Eq. (19), S_q is governed by the off-diagonal density matrix elements $\rho_{n,n-1}$; $\langle \hat{a}^\dagger \hat{a} \rangle$, in contrast, is governed by the diagonal density matrix elements $\rho_{n,n}$. Since the off-diagonal elements of the density matrix, which determine the phase localization, are within first-order perturbation theory proportional to Ω (see Appendix B), with a proportionality factor that depends

on the $\rho_{n,n}$ and $\rho_{n,n+2}$ ($n = 1, 2, \ldots$) elements, it should, however, not be a surprise that $\bar{S}_q$ (Fig. 4) and $\bar{N}$ (Fig. 5) display similar overall characteristics.

To quantify the deformation of the limit cycle due to the external drive, Fig. 6 shows the time-averaged deformation $\bar{D}$ for the same parameters as those employed in Figs. 4–6. Not surprisingly, the overall behavior of $\bar{D}$—just like that of $\bar{S}_q$ and $\bar{N}$—resembles an Arnold tongue. While the deformation is quite large for "large" drive strengths and "small" detunings, inspection of the Wigner functions shows that the limit cycle is not broken, i.e., the maximum of the Wigner function still follows the shape of the zero-drive limit cycle, though with increased amplitude. Even though the deformation $\bar{D}$ is appreciable, we are operating in a regime where the phase localization is intimately connected to the zero-drive limit cycle.

Next, we discuss the spectral response. The spectra shown in Figs. 7 and 8 are calculated within the RWA in the frame that rotates at the drive frequency. We use Eq. (20) with $\tau = 200$ and simulation parameters that yield $\omega \in [-3, 3]$ with a frequency resolution of $1/500$. Consistent with the $\Omega = 0$ limit cycle discussion presented earlier, $S_p(\omega, \tau)$ is independent of τ for the RvdP oscillator (middle column of Figs. 7 and 8) but displays, in general, a dependence on τ for the R and vdP oscillators (left and right columns of Figs. 7 and 8). The τ dependence tends to be weak (similar behavior was observed in Ref. [7]; see also discussion below).

The top row of Fig. 7 shows the power spectrum for the R, RvdP, and vdP oscillators in the quantum regime as functions of ω and Δ [the linear and nonlinear parameters are the same as those employed in Figs. 4(k), 4(m), and 4(o)]. We note that beyond-RWA terms, which are not included in the calculations, might play a non-negligible role for the larger $|\Delta|$. The spectra are, for each Δ, normalized such that the maximum of the broad peak that is centered at $\omega \approx \Delta$ is equal to 1. For all Δ considered, the height of the δ-function-like peak is larger than 1, i.e., the value of this sharp spike is capped for visualization purposes. The red (lowest) curves in Figs. 7(d)–7(f) correspond to horizontal $\Delta = 0$ cuts through the data shown in Figs. 4(k), 4(m), and 4(o). For comparison, the green (middle) curves and blue (top) curves show $\Delta = 0$ spectra for the intermediate and classical regimes, respectively, using the same nonlinear parameters as in Figs. 4(f), 4(h), 4(j), 4(a), 4(c), and 4(e). Unlike in the top row, the maximum of the broad peak is not scaled to 1 in the bottom row of Fig. 7. Moreover, the δ-function-like spike (a single data point at $\omega = 0$) is taken out by hand. For comparison, Fig. 8 shows the power spectra $S_p(\omega, \tau)$ for a finite detuning, namely $\Delta = 1/20$, and two different drive strengths ($\Omega = 3\sqrt{2}/5 \approx 0.849$ and $\sqrt{2}/5 \approx 0.283$ for the top and bottom rows, respectively) using the same linear and nonlinear parameters as well as the same color coding as Fig. 7. The insets of Fig. 8 omit the δ-function-like spike and normalize, as in the top row of Fig. 7, the spectra such that the broad peak has a height of 1. The insets allow one to read off at which ω the maximum of the broad peak is located.

The key characteristics of the power spectra are the following: (i) The very sharp peak centered at $\omega = 0$ (top row of Fig. 7 and main panels of Fig. 8) exists for all three oscillator types; since we are working in the frame that rotates with the drive frequency, this peak reflects a strong response at the frequency corresponding to the drive. (ii) The broad peak centered at $\omega \approx \Delta$ (see, e.g., the bright red feature in the top row of Fig. 7) exists for all three oscillator types; this broad peak can be interpreted as a strong response, broadened by the dissipative processes, around the natural harmonic oscillator frequency. As discussed in more detail below, the maximum of this broad peak is, in general, not located at $\omega = 0$; thus, true entrainment is, in general, absent. (iii) The broad peak is narrower for the RvdP oscillator than for the R and vdP oscillators. Moreover, the broadness of the peak depends rather weakly on Δ. (iv) The broad peak centered at $\omega \approx \Delta$ is broader in the quantum regime than in the classical regime for all oscillator types. This is attributed to the increase of the zero-point motion in the quantum regime [8,10]. (v) The R and vdP oscillators feature sharp peaks, corresponding to higher harmonics, that are centered at $\omega = 2\Delta + 2$, $\omega = 2\Delta - 4$, and $\omega = 2\Delta - 2$ [in the quantum regime, this peak is hardly visible on the scale shown in Figs. 7(d) and 7(f)].

To gain insights into the existence or lack of entrainment for small $|\Delta|$, we investigate the difference between the frequency ω_{obs}, at which the broad peak that is centered around $\omega \approx \Delta$ takes its maximum, and the detuning Δ. This difference can be read off the spectra, such as those shown in Figs. 7(d)–7(f) for zero detuning and the insets of Fig. 8 for finite detuning. The main panel of Fig. 9 shows ω_{obs} as a function of the drive strength Ω for the RvdP oscillator in the quantum, transition, and classical regimes [curves from bottom (blue) to top (red)] for the same linear and non'linear parameters as used in the middle columns of Figs. 7 and 8. For all three regimes, ω_{obs} is equal to Δ for $\Omega = 0$ (in the absence of the drive, the spectral response is maximal at the natural harmonic oscillator frequency) and decreases monotonically with increasing Ω. Even though ω_{obs} tends toward zero, especially in the classical regime (a value of $\omega_{\text{obs}} = 0$ would indicate entrainment), true entrainment is absent for the oscillator strengths considered. The drive strength was not increased further since we wish to remain in the weakly perturbed regime, where the driven system inherits key characteristics of the limit-cycle state of the undriven system.

To further explore the presence or absence of entrainment, the inset of Fig. 9 shows $\omega_{\text{obs}} - \Delta$ as a function of the detuning for the RvdP oscillator. Using ω_{obs}, as was done in Ref. [10], as a proxy for the frequency at which the system responds, entrainment would correspond to $\omega_{\text{obs}} - \Delta$ following the dashed line. It can be seen that entrainment exists, for sufficiently small Δ, in the classical regime but not in the quantum regime (of course, we cannot rule out the existence of entrainment in this regime for $|\Delta|$ values that are below our resolution scale). The observation of entrainment in the classical regime is consistent with results presented in Ref. [10]. The "oscillatory" behavior of $\omega_{\text{obs}} - \Delta$ in the quantum regime is interpreted as reflecting an appreciable "hybridization" of the spectral function with regards to the drive and oscillator frequencies. This deep quantum regime has not, to the best of our knowledge, been investigated previously.
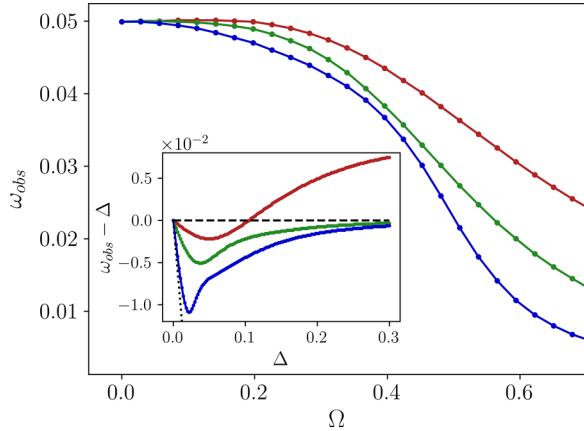
FIG. 9. Analysis of the maximum of the broad peak for the RvdP oscillator for $\tau = 200$. Main panel: Blue (bottom), green (middle), and red (top) curves show the location ω_{obs} of the maximum of the broad peak for the classical regime, transition regime, and quantum regime, respectively, as a function of the drive strength Ω for $\Delta = 1/20$. The linear parameters are $\gamma_1^+ = 1/5$ and $\gamma_1^- = 1/10$ while the nonlinear parameters for the red (bottom) curve, green (middle) curve, and blue (top) curve are given in Table I(m), I(h), and I(c), respectively. The calculations are performed within the RWA in the frame that rotates at the drive frequency. Inset: Blue (bottom), green (middle), and red (top) curves show the shifted location $\omega_{obs} - \Delta$ of the maximum of the broad peak for the classical regime, transition regime, and quantum regime, respectively, as a function of the detuning Δ for $\Omega = 3/10$ (the other parameters are the same as those in the main panel). If $\omega_{obs} - \Delta$ followed the black dotted line, the system would exhibit true entrainment. On the other hand, if $\omega_{obs} - \Delta$ followed the black dashed line, the system response would be governed by the natural harmonic oscillator frequency.

We finish this section by highlighting a few key aspects of driven generalized RvdP oscillators in the deep quantum regime, for which the number of excitations of the undriven limit cycle state is notably smaller than 1. In this "extreme" quantum regime, none of the oscillators exhibits entrainment for the parameter combinations considered. While the power spectra of the driven RvdP oscillator show fairly symmetric broadened peaks, the spectra of the driven R and vdP oscillators, which are characterized by phase-space asymmetric dissipators, show more structure, suggesting a stronger dissipation-induced hybridization of the drive and natural oscillator frequencies. It is suggested that these phase-space asymmetric oscillators are most meaningfully characterized by the entire power spectrum: extracting a single number, such as ω_{obs}, tends to provide a rather incomplete characterization of the system. In the limit where the broad peak is comparatively narrow (i.e., where the peak width is smaller than or of the same order of magnitude as $|\Delta|$), in contrast, ω_{obs} is a reliable indicator of entrainment.

IV. CONCLUSIONS

This paper presented a detailed analysis of the driven generalized Rayleigh-van der Pol oscillators—including the driven Rayleigh (R), driven Rayleigh-van der Pol (RvdP), and driven van der Pol (vdP) oscillators—within a master

equation framework. While the drive was treated classically, the motional degrees of freedom of the oscillator were quantized, with linear and nonlinear loss/gain accounted for through dissipators. In the weak ϵ limit (i.e., for small effective linear loss or gain), a mapping to the classical equations of motion was established. The mapping allows for a transparent interpretation of the dissipative terms. An important aspect of the generalized RvdP oscillator is that the dissipators are not, in general, rotationally symmetric in phase space. As a consequence, the drive-free Wigner functions exhibit a phase-space asymmetry that increases with decreasing number $\bar{N}$ of excitations. Our main focus throughout was to characterize the quasistationary long-time regime, where the dynamics is linked to the limit cycle of the undriven system; this limit cycle emerges due to the competition between linear and nonlinear dissipative processes.

In classical settings, phase localization and frequency entrainment are critical elements for harnessing characteristics associated with limit cycles; correspondingly, classical synchronization is defined as requiring phase localization and frequency entrainment. By analogy, we defined quantum synchronization as requiring phase localization and frequency entrainment. Our analysis shows that the driven generalized RvdP oscillators exhibit Arnold-like synchronization tongues. This work employed a phase operator-based definition for the phase localization measure S_q. Observables such as the excitation number and the deformation of the limit cycle were found to exhibit analogous Arnold-tongue shaped characteristics, if plotted as functions of the detuning and drive strength. Phase localization was found to decrease for all oscillator types considered as the system changed from the classical to the quantum regime. The phase space asymmetry of the non-RvdP oscillators was found to reduce phase localization. In the quantum regime, where the number of excitations $\bar{N}$ is low, the spectral response of the systems was found to be extremely broad, suggesting that the frequency at which the non-delta-function response of the spectrum is maximal provides only limited information about the system's response. While appreciable phase space localization was observed in the deep quantum regime, weak frequency entrainment was only found for the RvdP oscillator in the deep quantum regime, and only for a narrow range of small, in absolute value, detunings. We were not able to identify a parameter combination in the deep quantum regime where the driven generalized RvdP oscillator exhibits true nontrivial synchronization, i.e., phase localization and frequency locking to the drive.

Our analysis and findings suggest a number of follow-up studies. It would be interesting to investigate whether specifically designed driving protocols could be used to identify parameter regimes where the driven generalized RvdP oscillators exhibit synchronization. Such protocols could, e.g., be developed by allowing for a time-dependent drive frequency that may be constructed from trajectories such as those presented in Figs. 3(a) and 3(c). Since phase-space asymmetries may be encountered in a range of realistic systems, the targeted design of driving protocols may have practical applications. Another interesting direction is to explore the characteristics of a network of generalized RvdP oscillators without an external drive. It would, e.g., be interesting to explore if dissipation-driven synchronization exists in this

network either for linear or nonlinear nondissipative coupling between the oscillators.

APPENDIX A: MASTER EQUATION IN THE ROTATING FRAME

To get started, we introduce the rotation operator $\hat{U}(t)$,

$$\hat{U}(t) = e^{-\iota \omega_R \hat{a}^\dagger \hat{a} t}, \tag{A1}$$

where the angular frequency ω_R could be equal to the angular frequency of the harmonic oscillator (which is equal to 1 in the dimensionless units employed throughout), the angular frequency ω_D of the drive, or some other angular frequency. The operator $\hat{C}$ in the rotating frame is denoted by $\hat{C}_R$,

$$\hat{C}_R = \hat{U}^\dagger(t) \hat{C} \hat{U}(t). \tag{A2}$$

For the driving term, one finds

$$(\hat{V}_{\text{drive}})_R = \frac{\Omega}{2\iota\sqrt{2}}(e^{\iota(\omega_D - \omega_R)t}\hat{a} - e^{-\iota(\omega_D - \omega_R)t}\hat{a}^\dagger)$$
$$+ \frac{\Omega}{2\iota\sqrt{2}}(e^{\iota(\omega_D + \omega_R)t}\hat{a}^\dagger - e^{-\iota(\omega_D + \omega_R)t}\hat{a}), \tag{A3}$$

where the terms on the right-hand side correspond to terms within the RWA (first line) and terms beyond the RWA (second line), respectively.

The master equation in the frame rotating with angular frequency ω_R reads

$$\dot{\rho}_R = -\iota[(1 - \omega_R)\hat{H}_0 + (\hat{V}_{\text{drive}})_R, \hat{\rho}_R]$$
$$+ \gamma_1^+ \hat{\mathcal{D}}[\hat{a}_R^\dagger](\hat{\rho}_R) + \gamma_1^- \hat{\mathcal{D}}[\hat{a}_R](\hat{\rho}_R) + \alpha\hat{\mathcal{D}}[\hat{a}_R\hat{a}_R](\hat{\rho}_R)$$
$$+ \beta\hat{\mathcal{D}}[\hat{x}_R\hat{a}_R](\hat{\rho}_R) + \delta\hat{\mathcal{D}}[\hat{p}_R\hat{a}_R](\hat{\rho}_R), \tag{A4}$$

where

$$\hat{\mathcal{D}}[\hat{C}_R](\hat{\rho}_R) = \hat{U}^\dagger(t)\hat{\mathcal{D}}[\hat{C}](\hat{\rho})\hat{U}(t). \tag{A5}$$

It is readily shown that the form of the dissipators that are proportional to γ_1^+, γ_1^-, and γ_2 is the same in the rotating frame as in the laboratory frame:

$$\hat{\mathcal{D}}[\hat{a}_R](\hat{\rho}_R) = \hat{\mathcal{D}}[\hat{a}](\hat{\rho}_R), \tag{A6}$$

$$\hat{\mathcal{D}}[\hat{a}_R^\dagger](\hat{\rho}_R) = \hat{\mathcal{D}}[\hat{a}^\dagger](\hat{\rho}_R), \tag{A7}$$

and

$$\hat{\mathcal{D}}[\hat{a}_R\hat{a}_R](\hat{\rho}_R) = \hat{\mathcal{D}}[\hat{a}\hat{a}](\hat{\rho}_R). \tag{A8}$$

By "same form" ("different form") we mean that the argument of $\hat{\mathcal{D}}$ takes the same form (a different form) in the rotating frame as that in the laboratory frame. The dissipators that are proportional to β and δ, in contrast, take a different form in the rotating frame than in the laboratory frame:

$$\hat{\mathcal{D}}[\hat{x}_R\hat{a}_R](\hat{\rho}_R) = \hat{\mathcal{D}}[(\hat{x} + \hat{y} + \hat{y}^\dagger)\hat{a}](\hat{\rho}_R) \tag{A9}$$

and

$$\hat{\mathcal{D}}[\hat{p}_R\hat{a}_R](\hat{\rho}_R) = \hat{\mathcal{D}}[(\hat{p} - \iota(\hat{y} - \hat{y}^\dagger))\hat{a}](\hat{\rho}_R), \tag{A10}$$

where the time-dependent operator $\hat{y}$ is defined as

$$\hat{y}(t) = \frac{1}{\sqrt{2}}[\exp(-\iota\omega_R t) - 1]\hat{a}. \tag{A11}$$

The appearance of the operators $\hat{y}$ and $\hat{y}^\dagger$ may be interpreted as being due to a fictitious force in the rotating frame. For in-depth discussions of the connection between the laboratory- and rotating-frame master equations, the reader is referred to Refs. [43–45].

APPENDIX B: PHASE LOCALIZATION MEASURES

Several quantum phase localization measures have been proposed (see, e.g., Refs. [13,17,22,25,35,36,46–49]), including measures based on the phase operator and quantum information theory frameworks, not only in the context of different oscillator types—as considered in this work—but also in the context of spin systems [16,17,20,50–56]. This Appendix provides more context for the phase localization measure S_q, Eq. (18), employed in this work and relates it to other phase operator based measures.

The phase operator $\hat{\varphi}$ is defined through $\hat{\varphi}|\varphi\rangle = \varphi|\varphi\rangle$, where the phase state $|\varphi\rangle$ is a superposition of the harmonic oscillator eigenstates $|n\rangle$ [37],

$$|\varphi\rangle = \frac{1}{\sqrt{2\pi}}\sum_{n=0}^{\infty}\exp(\iota n\varphi)|n\rangle. \tag{B1}$$

Using the properties of the phase states, Eq. (19) follows readily from Eq. (18).

An alternative phase localization measure reads $S_{\text{q,alter1}} = \text{Re}(\langle\hat{a}\rangle)/|\langle\hat{a}\rangle|$ [40], where $\text{Re}(C)$ denotes the real part of C. Writing $\langle\hat{a}\rangle$ in terms of the amplitude $|a|$ and phase φ [namely, $\langle\hat{a}\rangle = |a|\exp(-\iota\varphi)$] highlights that $\langle\hat{a}\rangle$ contains phase information. Evaluating $S_{\text{q,alter1}}$ in the harmonic oscillator basis, one finds

$$S_{\text{q,alter1}} = \frac{\text{Re}\left(\sum_{n=1}^{\infty}\sqrt{n}\rho_{n,n-1}\right)}{\left|\sum_{n=1}^{\infty}\sqrt{n}\rho_{n,n-1}\right|}. \tag{B2}$$

Equation (B2) shows that the density matrix elements that contribute to $S_{\text{q,alter1}}$ are the same as those that contribute to

S_q; the density matrix elements are, however, weighted differently. Use of the imaginary part of $\langle \hat{a} \rangle$ yields complementary insights [40].

We note that $S_{q,\text{alter1}}$ can, in the small Ω limit, be related to the susceptibility χ [27],

$$\chi = \frac{\partial \langle \hat{a} \rangle}{\partial \Omega}. \tag{B3}$$

To see the connection between $S_{q,\text{alter1}}$ and χ, we employ the perturbation theory framework detailed in Ref. [20]. When the $\Omega = 0$ steady state density matrix is used as zeroth-order solution and the external drive in the RWA is treated as a perturbation, $\langle \hat{a} \rangle$ is directly proportional to Ω. It follows that $S_{q,\text{alter1}}$ is equal to $\text{Re}(\Omega \chi)/|\langle \hat{a} \rangle|$ in the weakly driven regime, where first-order perturbation theory provides a faithful description. This indicates that the susceptibility results for the driven RvdP oscillator for small Ω [27] can be interpreted within the framework of phase localization. Note, however, that since phase localization requires the presence of a nonlinearity, only the results from Ref. [27] for nonvanishing nonlinearity can be meaningfully reinterpreted in this way.

Phase localization can also be defined in terms of the normalized phase probability $P(\varphi)$ [16],

$$P(\varphi) = \int_0^{2\pi} \delta(\varphi - \varphi') \langle \varphi' | \hat{\rho} | \varphi' \rangle d\varphi'. \tag{B4}$$

Using the maximum of the normalized phase probability, the phase localization measure $S_{q,\text{alter2}}$, which is frequently used in the context of spin systems, reads [16]

$$S_{q,\text{alter2}} = 2\pi \max_\varphi P(\varphi) - 1. \tag{B5}$$

Since $\langle \hat{\rho} \rangle$ is equal to 1, $S_{q,\text{alter2}}$ reduces to

$$S_{q,\text{alter2}} = \max_\varphi \sum_{k \neq l} \exp[-\iota(k - l)\varphi] \rho_{k,l}. \tag{B6}$$

Using that $\rho_{k,l}$ is equal to $(\rho_{l,k})^*$, it can be shown readily that $S_{q,\text{alter2}}$ is real. Physically, $S_{q,\text{alter2}}$ can be thought of as extracting the maximal height of $P(\varphi)$. Note that $S_{q,\text{alter2}}$ is sensitive to all off-diagonal density matrix elements. Specifically, the operation $\max_\varphi$ "optimizes" the multiplicative factor of the sum of the density matrix elements with $|k - l| = 1$ [multiplicative factor is $\exp(\iota\varphi)$], $|k - l| = 2$ [multiplicative factor is $\exp(2\iota\varphi)$], and so on.

We now discuss the $\beta = \delta$ oscillator, treating the drive in the RWA [see Eq. (7)], in more detail. For the arguments that follow, it is convenient to work in the frame that is rotating with the external drive. For $\beta = \delta$, the $\Omega = 0$ steady state density matrix $\rho^{(0)}$ is diagonal, as already mentioned in Sec. II. It is determined by $\hat{\mathcal{L}}_0 \hat{\rho}^{(0)} = 0$, where $\hat{\mathcal{L}}_0$ denotes the superoperator that corresponds to the $\Omega = 0$ master equation [20]. The first-order density matrix $\hat{\rho}^{(1)}$ is obtained by solving $\hat{\mathcal{L}}_{\text{drive}} \hat{\rho}^{(0)} = -\hat{\mathcal{L}}_0 \hat{\rho}^{(1)}$, where the superoperator $\hat{\mathcal{L}}_{\text{drive}}$ is fully determined by the external drive [20]. It can be readily shown that the only nonzero elements of $\hat{\rho}^{(1)}$ are those with $|k - l| = 1$. Consequently, $S_{q,\text{alter2}}$ reduces to $2\max_\varphi[\text{Re}(\cos\varphi \sum_{n=1}^\infty \rho_{n,n-1}) + \text{Im}(\sin\varphi \sum_{n=1}^\infty \rho_{n,n-1})]$. This shows that S_q, $S_{q,\text{alter1}}$, and $S_{q,\text{alter2}}$ are all governed by the same matrix elements.

Releasing the restriction that Ω is small while continuing to focus on the RvdP oscillator ($\beta = \delta$), another interesting limit is the deep quantum regime (characterized by small $\langle \hat{a}^\dagger \hat{a} \rangle$), where the full steady state density matrix elements are well approximated by a three-state model [21]. Within the three-state model, the only nonzero off-diagonal elements are $\rho_{1,0} = (\rho_{0,1})^*$. Correspondingly, S_q, $S_{q,\text{alter1}}$, and $S_{q,\text{alter2}}$ are related to each other in a straightforward manner.

[1] A. Pikovsky, M. Rosenblum, and J. Kurths, *Synchronization, A Universal Concept in Nonlinear Sciences* (Cambridge University Press, Cambridge, 2001).

[2] A. Balanov, N. Janson, D. Postnov, and O. Sosnovtseva, *Synchronization* (Springer, Berlin, 2009).

[3] J. W. Strutt and B. Rayleigh, On maintained vibrations, Philos. Mag. **15**, 229 (1883).

[4] B. van der Pol Jun, Forced oscillators in a circuit with non-linear resistance. (Reception with reactive triode), Philos. Mag. **3**, 65 (1927).

[5] B. van der Pol and J. van der Mark, The heartbeat considered as a relaxation oscillation, and an electrical model of the heart, Philos. Mag. Suppl. **6**, 763 (1928).

[6] We start with the differential equation for the Rayleigh oscillator [Eq. (15) with $\Omega = \bar{\gamma}_{2,\text{vdp}} = 0$]. Differentiation with respect to time yields $\dddot{x} + \dot{x} = \epsilon(1 - 3\bar{\gamma}_{2,\text{ray}}\dot{x}^2)\ddot{x}$. Defining

$\bar{\gamma}_{2,\text{vdp}} = 3\bar{\gamma}_{2,\text{ray}}$ and making the substitution $y = \dot{x}$, one obtains the differential equation for the van der Pol oscillator.

[7] A. Chia, L. C. Kwek, and C. Noh, Relaxation oscillations and frequency entrainment in quantum mechanics, Phys. Rev. E **102**, 042213 (2020).

[8] L. Ben Arosh, M. C. Cross, and R. Lifshitz, Quantum limit cycles and the Rayleigh and van der Pol oscillators, Phys. Rev. Res. **3**, 013130 (2021).

[9] T. E. Lee and H. R. Sadeghpour, Quantum synchronization of quantum van der Pol oscillators with trapped ions, Phys. Rev. Lett. **111**, 234101 (2013).

[10] S. Walter, A. Nunnenkamp, and C. Bruder, Quantum synchronization of a driven self-sustained oscillator, Phys. Rev. Lett. **112**, 094102 (2014).

[11] N. Lörch, S. E. Nigg, A. Nunnenkamp, R. P. Tiwari, and C. Bruder, Quantum synchronization blockade: Energy

quantization hinders synchronization of identical oscillators, Phys. Rev. Lett. **118**, 243602 (2017).

[12] L. Morgan and H. Hinrichsen, Oscillation and synchronization of two quantum self-sustained oscillators, J. Stat. Mech.: Theory Exp. (2015) P09009.

[13] T. E. Lee, C.-K. Chan, and S. Wang, Entanglement tongue and quantum synchronization of disordered oscillators, Phys. Rev. E **89**, 022913 (2014).

[14] E. Amitai, N. Lørch, A. Nunnenkamp, S. Walter, and C. Bruder, Synchronization of an optomechanical system to an external drive, Phys. Rev. A **95**, 053858 (2017).

[15] E. Amitai, M. Koppenhøfer, N. Lørch, and C. Bruder, Quantum effects in amplitude death of coupled anharmonic self-oscillators, Phys. Rev. E **97**, 052203 (2018).

[16] M. R. Hush, W. Li, S. Genway, I. Lesanovsky, and A. D. Armour, Spin correlations as a probe of quantum synchronization in trapped-ion phonon lasers, Phys. Rev. A **91**, 061401(R) (2015).

[17] V. Ameri, M. Eghbali-Arani, A. Mari, A. Farace, F. Kheirandish, V. Giovannetti, and R. Fazio, Mutual information as an order parameter for quantum synchronization, Phys. Rev. A **91**, 012301 (2015).

[18] T. Weiss, S. Walter, and F. Marquardt, Quantum-coherent phase oscillations in synchronization, Phys. Rev. A **95**, 041802(R) (2017).

[19] S. Sonar, M. Hajdušek, M. Mukherjee, R. Fazio, V. Vedral, S. Vinjanampathy, and L.-C. Kwek, Squeezing enhances quantum synchronization, Phys. Rev. Lett. **120**, 163601 (2018).

[20] M. Koppenhöfer and A. Roulet, Optimal synchronization deep in the quantum regime: Resource and fundamental limit, Phys. Rev. A **99**, 043804 (2019).

[21] W.-K. Mok, L.-C. Kwek, and H. Heimonen, Synchronization boost with single-photon dissipation in the deep quantum regime, Phys. Rev. Res. **2**, 033422 (2020).

[22] N. Jaseem, and M. Hajdušek, P. Solanki, L.-C. Kwek, R. Fazio, and S. Vinjanampathy, Generalized measure of quantum synchronization, Phys. Rev. Res. **2**, 043287 (2020).

[23] J. Li, C. Ding, and Y. Wu, Highly nonclassical phonon emission statistics through two-photon loss of van der Pol oscillator, J. Appl. Phys. **128**, 234302 (2020).

[24] A. Cabot, G. C. Giorgi, and R. Zambrini, Metastable quantum entrainment, New J. Phys. **23**, 103017 (2021).

[25] N. Thomas and M. Senthilvelan, Quantum synchronization in quadratically coupled quantum van der Pol oscillators, Phys. Rev. A **106**, 012422 (2022).

[26] N. Es'haqi-Sani, G. Manzano, R. Zambrini, and R. Fazio, Synchronization along quantum trajectories, Phys. Rev. Res. **2**, 023101 (2020).

[27] S. Dutta and N. R. Cooper, Critical response of a quantum van der Pol oscillator, Phys. Rev. Lett. **123**, 250401 (2019).

[28] H. D. Simaan and R. Loudon, Quantum statistics of single-beam two-photon absorption, J. Phys. A: Math. Gen. **8**, 539 (1975).

[29] V. V. Dodonov and S. S. Mizrahi, Exact stationary photon distributions due to competition between one- and two-photon absorption and emission, J. Phys. A: Math. Gen. **30**, 5657 (1997).

[30] The master equation for $\beta = \delta \neq 0$ is equivalent to that for $\beta = \delta = 0$ and modified α: $\alpha \to \alpha + \beta/2 + \delta/2 = \alpha + \beta$.

[31] M. O. Scully and M. S. Zubairy, *Quantum Optics*, 1st ed. (Cambridge University Press, Cambridge, 1997).

[32] C. M. Bender and S. A. Orszag, *Advanced Mathematical Methods for Scientists and Engineers: Asymptotic Methods and Perturbation Theory* (Springer, Berlin, 1999).

[33] T. D. Burton, A perturbation method for certain non-linear oscillators, Int. J. Non Linear Mech. **19**, 397 (1984).

[34] H. Goldstein, C. Poole, and J. Safko, *Classical Mechanics*, 3rd ed. (Addison-Wesley, Reading, MA, 2005).

[35] A. Mari, A. Farace, N. Didier, V. Giovannetti, and R. Fazio, Measures of quantum synchronization in continuous variable systems, Phys. Rev. Lett. **111**, 103605 (2013).

[36] J. Tindall, C. Sánchez Muñoz, B. Buča, and D. Jaksch, Quantum synchronization enabled by dynamical symmetries and dissipation, New J. Phys. **22**, 013026 (2020).

[37] D. T. Pegg and S. M. Barnett, Unitary phase operator in quantum mechanics, Europhys. Lett. **6**, 483 (1988).

[38] J. H. Shapiro and S. R. Shepard, Quantum phase measurement: A system-theory perspective, Phys. Rev. A **43**, 3795 (1991).

[39] H. Breuer and F. Petruccione, *The Theory of Open Quantum Systems* (Oxford University Press, New York, 2002).

[40] T. Weiss, A. Kronwald, and F. Marquardt, Noise-induced transitions in optomechanical synchronization, New J. Phys. **18**, 013043 (2016).

[41] S. André, L. Guo, V. Peano, M. Mathaler, and G. Schøn, Emission spectrum of the driven nonlinear oscillator, Phys. Rev. A **85**, 053825 (2012).

[42] T. E. Lee and M. C. Gross, Quantum-classical transition of correlations of two coupled cavities, Phys. Rev. A **88**, 013834 (2013).

[43] G. Shavit, B. Horowitz, and M. Goldstein, Bridging between laboratory and rotating-frame master equations for open quantum systems, Phys. Rev. B **100**, 195436 (2019).

[44] W. J. Munro and C. W. Gardiner, Non-rotating-wave master equation, Phys. Rev. A **53**, 2633 (1996).

[45] B. Baker, A. C. Y. Li, N. Irons, N. Earnest, and J. Koch, Adaptive rotating-wave approximation for driven open quantum systems, Phys. Rev. A **98**, 052111 (2018).

[46] F. Galve, G.-L. Giorgi, and R. Zambrini, Quantum correlations and synchronization measures, in *Lectures on General Quantum Correlations and Their Applications*, edited by F. F. Fanchini, D. D. O. S. Pinto, and G. Adesso (Springer, Berlin, 2017), pp. 393–420.

[47] H. Heimonen, L. C. Kwek, R. Kaiser, and G. Labeyrie, Synchronization of a self-sustained cold-atom oscillator, Phys. Rev. A **97**, 043406 (2018).

[48] R. Barak and Y. Ben-Aryeh, Non-orthogonal positive operator valued measure phase distributions of one- and two-mode electromagnetic fields, J. Opt. B: Quantum Semiclass. Opt. **7**, 123 (2005).

[49] O. V. Zhirov and D. L. Shepelyansky, Quantum synchronization, Eur. Phys. J. D **38**, 375 (2006).

[50] I. Goychuk, J. Casado-Pascual, M. Morillo, J. Lehmann, and P. Hänggi, Quantum stochastic synchronization, Phys. Rev. Lett. **97**, 210601 (2006).

[51] O. V. Zhirov and D. L. Shepelyansky, Synchronization and bistability of a qubit coupled to a driven dissipative oscillator, Phys. Rev. Lett. **100**, 014101 (2008).

[52] M. Xu, D. A. Tieri, E. C. Fine, J. K. Thompson, and M. J. Holland, Synchronization of two ensembles of atoms, Phys. Rev. Lett. **113**, 154101 (2014).

[53] G. L. Giorgi, F. Plastina, G. Francica, and R. Zambrini, Spontaneous synchronization and quantum correlation dynamics of open spin systems, Phys. Rev. A **88**, 042115 (2013).

[54] A. Roulet and C. Bruder, Synchronizing the smallest possible system, Phys. Rev. Lett. **121**, 053601 (2018).

[55] A. Roulet and C. Bruder, Quantum synchronization and entanglement generation, Phys. Rev. Lett. **121**, 063601 (2018).

[56] R. Tan, C. Bruder, and M. Koppenhøfer, Half-integer vs. integer effects in quantum synchronization of spin systems, Quantum **6**, 885 (2022).